

## ENCLOSURE 2

MFN 10-119

### Void Fraction Uncertainty Based on 10x10 Fuel Pressure Drop Data NEDO-33173 Supplement 1 Revision 0 April 2010

Non-Proprietary Information

#### IMPORTANT NOTICE

Enclosure 2 is a non-proprietary version of Void Fraction Uncertainty Based on 10x10 Fuel Pressure Drop Data, NEDC-33173P Supplement 1 Revision 0, April 2010 from Enclosure 1, which has the proprietary information removed. Portions that have been removed are indicated by open and closed double brackets as shown here [[            ]].



**HITACHI**

GE Hitachi Nuclear Energy

NEDO-33173 Supplement 1

Revision 0

DRF Section 0000-0115-3575

Class I

April 2010

## **Licensing Topical Report**

# **VOID FRACTION UNCERTAINTY BASED ON 10X10 FUEL PRESSURE DROP DATA**

*Copyright 2010 GE-Hitachi Nuclear Energy Americas, LLC*

*All Rights Reserved*

## **NON-PROPRIETARY NOTICE**

This is a non-proprietary version of the document NEDC-33173P Supplement 1, Revision 0, from which the proprietary information has been removed. Portions of the document that have been removed are identified by white space within double square brackets, as shown here [[ ]].

## **IMPORTANT NOTICE REGARDING CONTENTS OF THIS REPORT**

### **Please Read Carefully**

The design, engineering, and other information contained in this document is furnished for the purpose(s) stated in the transmittal letter. The only undertakings of GEH with respect to information in this document are contained in the contracts between GEH and its customers or participating utilities, and nothing contained in this document shall be construed as changing that contract. The use of this information by anyone for any purpose other than that for which it is intended is not authorized; and with respect to any unauthorized use, GEH makes no representation or warranty, and assumes no liability as to the completeness, accuracy, or usefulness of the information contained in this document.

No use of or right to copy any of this information contained in this document, other than by the NRC and its contractors in support of GEH's application, is authorized except by contract with GEH, as noted above. The information provided in this document is part of and dependent upon a larger set of knowledge, technology, and intellectual property rights pertaining to the design of standardized, nuclear powered, electric generating facilities. Without access and a GEH grant of rights to that larger set of knowledge, technology, and intellectual property rights, this document is not practically or rightfully usable by others, except by the NRC or through contractual agreements with customers or participating utilities, as set forth in the previous paragraph.

## **Acknowledgments**

This document is the result of the technical contributions from many individuals and organizations in addition to the authors of this document. At the GE – Hitachi Nuclear Energy Americas LLC (GEH), significant contributions to the development of this document have been made by the following individuals: Jens Andersen, Belgacem Hizoum, and Brian Moore.

## TABLE OF CONTENTS

<b>1.0</b>	<b>INTRODUCTION AND OVERVIEW .....</b>	<b>1-1</b>
1.1	PURPOSE AND SCOPE .....	1-1
1.2	OVERVIEW OF THE DRIFT FLUX MODEL .....	1-2
1.3	THE FINDLAY-DIX CORRELATION AND DATABASE .....	1-3
1.3.1	<i>Pressure Drop Based Data .....</i>	<i>1-6</i>
1.4	APPLICATION OF THE FINDLAY-DIX CORRELATION .....	1-8
1.4.1	<i>Void Fraction Uncertainty Treatment .....</i>	<i>1-10</i>
1.4.2	<i>Application to ECCS-LOCA Models .....</i>	<i>1-11</i>
1.4.3	<i>Application to Transient Models .....</i>	<i>1-13</i>
1.5	FUEL THERMAL-HYDRAULIC TESTING .....	1-15
1.5.1	<i>New Design Features .....</i>	<i>1-15</i>
1.6	SUBCHANNEL VERSUS PLANAR AVERAGE VOID FRACTION .....	1-16
1.6.1	<i>In-Channel Void Distribution Model .....</i>	<i>1-17</i>
<b>2.0</b>	<b>COMPARISONS TO THERMAL-HYDRAULIC DATA.....</b>	<b>2-1</b>
2.1	PRESSURE DROP BIAS AND UNCERTAINTY .....	2-1
2.1.1	<i>Measurement Bias and Uncertainty .....</i>	<i>2-1</i>
2.1.2	<i>Calculational Bias and Uncertainty .....</i>	<i>2-1</i>
2.2	VOID FRACTION BIAS AND UNCERTAINTY .....	2-3
2.2.1	<i>Void Fraction Average Error or Bias .....</i>	<i>2-3</i>
2.2.2	<i>Void Fraction Uncertainty .....</i>	<i>2-5</i>
2.2.3	<i>Assumption Summary .....</i>	<i>2-6</i>
2.3	LOW FLOW RATE TEST RESULTS .....	2-7
2.3.1	<i>GE12 Low Flow Tests .....</i>	<i>2-16</i>
2.3.2	<i>GE14 Low Flow Tests .....</i>	<i>2-17</i>
2.3.3	<i>GNF2 Low Flow Tests .....</i>	<i>2-17</i>
2.3.4	<i>Low Flow Test Summary .....</i>	<i>2-18</i>
2.4	AN ALTERNATE APPROACH USING HIGH FLOW RATE TESTS .....	2-18
2.4.1	<i>Assumptions and Approach .....</i>	<i>2-18</i>
2.4.2	<i>Additional Test Results .....</i>	<i>2-19</i>
2.4.3	<i>Alternate Approach Summary .....</i>	<i>2-21</i>
2.5	COMPARISON SUMMARY .....	2-21
<b>3.0</b>	<b>BENCHMARK CALCULATIONS .....</b>	<b>3-1</b>
3.1	ALTERNATIVE APPROACHES TO VOID FRACTION PREDICTIONS .....	3-1
3.1.1	<i>The COBRAG Model .....</i>	<i>3-1</i>
3.1.2	<i>The TRACG Model .....</i>	<i>3-2</i>
3.2	BENCHMARK RESULTS .....	3-2
3.2.1	<i>OF-64 Data .....</i>	<i>3-2</i>
3.2.2	<i>NUPEC 8x8 Data .....</i>	<i>3-8</i>
3.2.3	<i>GNF2 10x10 Benchmark Comparisons .....</i>	<i>3-21</i>
3.3	BENCHMARK SUMMARY .....	3-24
<b>4.0</b>	<b>CONCLUSIONS.....</b>	<b>4-1</b>
4.1	SUMMARY .....	4-1
<b>5.0</b>	<b>REFERENCES .....</b>	<b>5-1</b>
<b>APPENDIX A</b>	<b>NOMENCLATURE AND ACRONYMS.....</b>	<b>A-1</b>
<b>APPENDIX B</b>	<b>ONE-DIMENSIONAL FLOW QUALITY, EQUILIBRIUM QUALITY, AND VOID FRACTION .....</b>	<b>B-1</b>

## TABLE OF CONTENTS

B.1	QUALITY .....	B-1
B.2	VOID FRACTION .....	B-2
B.3	APPLICATION TO FUEL SIMULATION .....	B-5
<b>APPENDIX C “METHOD B” PRESSURE DROP.....</b>		<b>C-1</b>
<b>APPENDIX D ATLAS MEASUREMENT UNCERTAINTIES .....</b>		<b>D-1</b>
<b>APPENDIX E STATISTICS .....</b>		<b>E-1</b>
E.1	OVERALL MEAN AND STANDARD DEVIATION BASED ON SUBSET VALUES.....	E-1
E.2	TOLERANCE INTERVALS .....	E-2
<b>APPENDIX F ERROR RESIDUALS AT HIGH FLOW RATES.....</b>		<b>F-1</b>
F.1	DISCUSSION.....	F-1
F.2	TREND ANALYSIS .....	F-1
F.3	CORRELATION ANALYSIS .....	F-3
F.4	INTEGRAL VERSUS LOCAL ERRORS.....	F-5

## LIST OF FIGURES

Figure 1-1	Void Quality Relation [12] .....	1-14
Figure 2-1	GE14 $\Delta P$ Versus Mass Flux For the 0 to 3 MWt Test Runs .....	2-8
Figure 2-2	Calculated $\delta\alpha$ Versus Quality By Bundle Segment ( $\Delta z$ ) .....	2-14
Figure 2-3	Calculated $\delta\alpha$ Versus Quality (from Figure 2-2) By Fuel Type .....	2-15
Figure 2-4	Example Calculated Void Profiles for GE14 Low Flow Tests.....	2-16
Figure 3-1	OF-64 Test 001 .....	3-4
Figure 3-2	OF-64 Test 013 .....	3-5
Figure 3-3	OF-64 Test 014 .....	3-6
Figure 3-4	OF-64 Test 019 .....	3-7
Figure 3-5	OF-64 Test 040 .....	3-8
Figure 3-6	Test Series 4101-39 Through 44 ( $G = 588 \text{ kg/m}^2\text{-s}$ ) .....	3-11
Figure 3-7	Test Series 4101-45 Through 50 ( $G = 878 \text{ kg/m}^2\text{-s}$ ) .....	3-12
Figure 3-8	Test Series 4101-54 Through 61 ( $G = 1,600 \text{ kg/m}^2\text{-s}$ ) .....	3-13
Figure 3-9	Test Series 4101-64 Through 68 ( $G = 2,040 \text{ kg/m}^2\text{-s}$ ) .....	3-14
Figure 3-10	Test Summary – Predicted Versus Measured Planar Average Void Fraction...	3-15
Figure 3-11	Predicted Versus Measured Radial Void Profiles ( $G = 588 \text{ kg/m}^2\text{-s}$ ) .....	3-16
Figure 3-12	Predicted Versus Measured Radial Void Profiles ( $G = 878 \text{ kg/m}^2\text{-s}$ ) .....	3-17
Figure 3-13	Predicted Versus Measured Radial Void Profiles ( $G = 1,600 \text{ kg/m}^2\text{-s}$ ) .....	3-18
Figure 3-14	Predicted Versus Measured Radial Void Profiles ( $G = 2,040 \text{ kg/m}^2\text{-s}$ ) .....	3-19
Figure 3-15	Quadrants for the Regional Void Fraction Asymmetry Evaluation .....	3-20
Figure 3-16	NUPEC Regional Void Fraction Asymmetry Versus Mass Flux.....	3-21
Figure 3-17	Predicted Void Fraction Trend for GNF2.....	3-23
Figure 3-18	GNF2 Void Fraction Predictions – Findlay-Dix vs. COBRAG .....	3-24
Figure B-1	Generic $MCPR_F$ .....	B-6
Figure B-2	Predicted Exit Void Fractions Based on Critical Power Data .....	B-7
Figure F-3	Predicted GE14 Bundle Pressure Drops Versus Data .....	F-2

## LIST OF FIGURES

Figure F-4	Pressure Drop Residual Error ( $\delta P$ ) Versus Power-to-Flow Ratio .....	F-4
Figure F-5	Pressure Drop Residual Error ( $\delta P$ ) Versus Mass Flux (G).....	F-5
Figure F-6	Pressure Drop and Void Fraction for Selected GNF2 Low Flow Tests .....	F-6
Figure F-7	Pressure Drop and Void Fraction for a High Exit Quality (Higher Flow) Test ..	F-7

## LIST OF TABLES

Table 1-1	Void Fraction – Original Findlay-Dix Multi-Rod Database .....	1-4
Table 1-2	Correlation Statistics for The Multi-Rod Database .....	1-5
Table 1-3	ASEA-813, 713 Statistics – Comparisons of 8x8 Low Flow Void Fraction Measurements Versus Findlay-Dix Predictions – 1,000 psia, $\Delta T_{\text{sub}} \sim 20$ °F, and Various Power Levels.....	1-7
Table 1-4	GE Methodologies That Employ the Findlay-Dix Correlation .....	1-8
Table 1-5	Values of Edge Rod Factors $k(x,y)$ Used in Equation (1.8) for Controlled Lattices.....	1-18
Table 1-6	Controlled Lattice Void Distribution Based on TGBLA.....	1-20
Table 1-7	Controlled Lattice Void Distribution Based on COBRAG .....	1-20
Table 1-8	Uncontrolled Lattice Void Distribution Based on TGBLA.....	1-21
Table 1-9	Uncontrolled Lattice Void Distribution Based on COBRAG .....	1-21
Table 2-1	GE12 (10x10) Thermal-Hydraulic Tests: ATA-365 and ATA-246 – Cosine APS .....	2-10
Table 2-2	GE14 (10x10) Thermal-Hydraulic Tests: STA-DP-GE14 Test Series With a Bottom Peaked APS .....	2-11
Table 2-3	GNF2 (10x10) Thermal-Hydraulic Tests: STA-DP-GNF2 Test Series With a Bottom Peaked APS .....	2-12
Table 2-4	GNF2 (10x10) Thermal-Hydraulic Tests: DP-GNF2-C1 Test Series With a Cosine APS.....	2-13
Table 2-5	10x10 Pressure Drop Test Conditions .....	2-20



## LIST OF TABLES

Table 2-6	10x10 Pressure Drop Test Data Summary .....	2-20
Table 3-1	Average Error ( $\Delta\alpha = \alpha_m - \alpha_c$ ) and Standard Deviation Comparisons for Planar Average Void Fractions.....	3-3
Table 3-2	BFBT Bundle Local Peaking Factor Array for Assembly #4 .....	3-9
Table 3-3	BFBT Test Series for Assembly 4 – Test Conditions .....	3-10
Table 3-4	GNF2 Benchmark Cases – Test Conditions .....	3-22
Table C-1	Expressions Applied to Calculate the In-Channel Pressure Drop .....	C-1

## **Abstract**

This document presents an overview of the Findlay-Dix void-quality correlation and its associated database, a review of its application in safety analysis methodologies, and the results of an analysis to evaluate the accuracy of the correlation as applied to GE 10x10 fuel designs. The correlation was developed in the mid-1970s based on a large body of experimental data that was available at the time. The analysis presented here is based on steady state pressure drop measurements taken from full-scale thermal-hydraulic tests using contemporary BWR fuel designs (10x10 arrays). Relating pressure drop error residuals to uncertainty in calculated void fraction provides a quantitative basis for evaluation. The results of this analysis indicate that the accuracy of the Findlay-Dix correlation is unchanged relative to its original validation basis when applied to current 10x10 fuel designs.

## 1.0 INTRODUCTION AND OVERVIEW

### 1.1 Purpose and Scope

GE<sup>1</sup> fuel product lines have continually evolved over the last 20 years, including innovations in spacer designs. Spacers provide a necessary mechanical function (e.g., support and separation of fuel pins), and play an important role in terms of critical power and pressure drop performance. Fuel critical power and pressure drop ( $\Delta P$ ) performance characteristics are experimentally confirmed from full-scale thermal-hydraulic testing, using electrically heated replicas of the fuel bundles. The pressure drop testing is used to determine or confirm spacer loss coefficients, which are ultimately used in design calculations and monitoring applications.

In order to model and predict pressure losses in a fuel bundle, the void fraction must be accurately predicted. The analytic expression used to evaluate the elevation pressure drop uses void fraction (directly) as a variable. Furthermore, in BWR applications such as a core simulator, the correct modeling of fuel pressure drop, flow rate, and axial power shape all depend on the accuracy of the void prediction due to the strong void/power feedback mechanism present in the reactor. One of GE's approved methods for predicting void fraction is the Findlay-Dix void correlation. The Findlay-Dix correlation is based on the drift-flux model. It is applied in one-dimension, providing a planar average void fraction as a function of steam properties (a function of temperature and pressure), quality, and a Reynolds number (dimensionless) based on the bundle flow rate. The Reynolds number, which represents the ratio of inertial to viscous forces, is calculated based on a characteristic length scale, i.e., the hydraulic diameter ( $D_H$ ).

The primary objective of this analysis is to assess the bias and uncertainty in the steady state void fraction values predicted by the Findlay-Dix correlation. The evaluation is based on comparisons of calculated  $\Delta P$  to the experimental  $\Delta P$  measurements obtained for the GE12, GE14, and GNF2 fuel bundle designs. These bundle designs represent a retired fuel product line, current (in-service) fuel, and a relatively new design, all of which are based on 10x10 lattices. The designs are comparable (axially dependent  $D_H \approx 0.40$  to 0.52 inches), but different with respect to the numbers, locations, and heights of the partial length fuel rods. The basis of this analysis is that uncertainty in the void prediction can be estimated by establishing a relationship between void fraction error and  $\Delta P$  error (calculated minus measured  $\Delta P$ ). The estimated error can then be compared with results from the original Findlay-Dix validation database in order to judge the adequacy of the correlation for 10x10 designs.

In general, it has been demonstrated that drift-flux type correlations predict both steady state and transient data well, including rapid transients [1]. However, transient void fraction prediction accuracy is not within the scope of this analysis and will only be briefly discussed in subsequent

---

<sup>1</sup> General Electric or simply "GE" is used in this document to refer to the GE Hitachi Nuclear Energy Americas, LLC ("GEH") and its affiliates, specifically Global Nuclear Fuel Americas, LLC (GNF-A).

sections. Transient void predictions are important for determining the correct dynamic response of reactor cores, as well as limiting channel performance. While transient two-phase flow predictions may utilize the void correlation, the adequacy of the results is also highly dependent on other factors, such as the formulation of the conservation equations, their numerical treatment, and other supporting models (e.g., heat transfer correlations, fuel-cladding gap conductance, fuel pin heat conduction, nuclear heat generation and direct moderator heating, etc.). Recognizing that these predictions are the product of a particular “equation and correlation set,” GE’s methodologies for transient and accident evaluations have their own qualification bases supporting regulatory approval. These bases support implementation of all the relevant models, including the drift flux model (void correlation) as appropriate.

## 1.2 Overview of the Drift Flux Model

The drift flux model is widely applied to predict two-phase flows. A brief review of the drift flux model and its basis is presented here. Defining the relative velocity between the phases as

$$u_{gf} = u_g - u_f = \frac{j_g}{\alpha} - \frac{j_f}{(1-\alpha)} \quad (1.1)$$

Clearing fractions gives an expression for the drift flux

$$j_{gf} = \alpha(1-\alpha)u_{gf} = j_g - \alpha j \quad (1.2)$$

The drift flux physically represents the volumetric rate that vapor passes through a unit of area in a plane normal to the direction of flow, where the plane is moving at the speed of the mixture,  $j$ . In order to preserve continuity, an equal and opposite drift flux of liquid must pass through the same plane. This relationship must be true for any unit area in the flow field (anywhere in the plane), regardless of the flow regime. Rearranging (1.2) and integrating over the channel flow area to define cross sectional averaged quantities gives

$$\frac{1}{A} \iint_A j_g dA = \frac{1}{A} \iint_A j_{gf} dA + \frac{1}{A} \iint_A \alpha j dA \quad (1.3)$$

$$\overline{j_g} = \overline{j_{gf}} + \overline{\alpha j} \quad (1.4)$$

For convenience, the distribution parameter and weighted mean drift velocity are defined

$$C_o = \frac{(\overline{\alpha j})}{(\overline{\alpha})(\overline{j})} \quad \text{and} \quad \overline{v_{gf}} = \frac{(\overline{j_{gf}})}{(\overline{\alpha})} \quad (1.5)$$

which can be substituted into (1.4) to give the familiar form of the drift flux model for one-dimensional two-phase flow.

$$\bar{\alpha} = \frac{\bar{j}_g}{C_o \bar{j} + \bar{v}_{gj}} \quad (1.6)$$

By definition,  $C_o$  and  $\bar{v}_{gj}$  are functions of the flow pattern (e.g., subcooled boiling, bubbly flow, churn, annular, etc.), degree of thermal equilibrium, channel characteristics, and total mass flow rate. These parameters are usually empirically correlated.

In Section 7.2.7 of the Safety Evaluation for NEDC-33173P [2], a concern was expressed for the effect of local peaking on the distribution parameter. It should be noted that the distribution parameter ( $C_o$ ) quantifies the effect of the radial void and volumetric flux distribution as a function of flow pattern (flow regime). In this sense,  $C_o$  is a measure of the global slip due to cross-sectional averaging and should not be considered to represent local (subchannel) effects. In the one-dimensional formulation of the drift flux model, the local information has essentially been lost. However, the usefulness of the drift flux model in many practical engineering systems comes from the fact that even two-phase mixtures that are weakly coupled locally can be considered, because the relatively large axial dimension of the systems usually gives sufficient interaction times [3].

The drift velocity,  $v_{gj}$ , is representative of the local slip and is closely related to the terminal rise velocity of the vapor phase through liquid [4]. For co-current up-flow conditions at relatively high void fractions characteristic of the annular flow regime, the total volumetric flux must approach the vapor volumetric flux as the void fraction increases, or  $\bar{j} \rightarrow \bar{j}_g$ ,  $\bar{v}_{gj} \rightarrow 0$ , and  $C_o \rightarrow 1$  as  $\alpha \rightarrow 1$ . At high void fractions, the Findlay-Dix correlated parameters behave (trend) as expected, consistent with the findings of other investigators [4], [5], [6]. More precisely, this behavior was actually a design constraint imposed to develop the correlation.

The drift flux model can be used with or without reference to any particular flow regime, as long as the base data used to correlate  $C_o$  and  $\bar{v}_{gj}$  are not restricted to a particular range. Ishii examined this issue directly [7], which is briefly discussed in Collier's textbook [8]. The Findlay-Dix correlation was developed considering data extending to very high void fractions [[ ]], covering the flow regimes from subcooled boiling well into annular flow, which avoids this potential limitation. In summary, there is no void fraction range restriction imposed on the application of the correlation.

### 1.3 The Findlay-Dix Correlation and Database

The Findlay-Dix correlation was introduced as GE's standard correlation for design application in the mid-1970s. Development of the correlation was initiated after inaccuracies in core physics predictions led to investigations of calculated fuel void fractions. The development program drove an expansion in the existing experimental database to include multi-rod datasets at typical BWR conditions. Under this program, data were obtained from experiments under contract at the Centro Informazione Studi Esperienze (CISE) laboratories in Italy and ASEA-Atom under a technical exchange agreement. This data was combined with GE's low flow database.

The Findlay-Dix correlation is presented in NEDE-21565 [9]. The correlation consists of a set of correlating parameters for  $C_o$  and  $\bar{v}_{gj}$  as a function of steam properties, Reynolds number, and void fraction. Using these functions and steam quality, Equation (1.6) can be directly solved for void fraction. Under steady state conditions, the steam quality is obtained from a simple energy balance (Appendix B).

The original multi-rod database is given in Table 1-1. The data is mainly comprised of 4x4, 6x6, 7x7, and 8x8 data. A variety of radial and axial power profiles, pressures, flow rates, and subcooling conditions were considered. Also, different measurement techniques were used in the various experiments. The CISE and GE datasets were based on integral techniques, i.e., inferring the void fraction from pressure drop information or direct measurement of the volume of fluid present in the two-phase mixture. The ASEA test series were based on a gamma-ray attenuation technique, where measurements were taken at various axial elevations in a test section (i.e., multiple test points were taken over the bundle length for a single test run).

The Findlay-Dix correlation has also been validated against a variety of simple geometry tests. These tests involved round tubes, annuli, and rectangular test sections. Furthermore, these tests extended the validation range in terms of thermal-hydraulic conditions (e.g., pressure, flow rates and steam qualities). The details of the simple geometry comparisons are presented in NEDE-21565.

**Table 1-1      Void Fraction – Original Findlay-Dix Multi-Rod Database**

<b>Source</b>	<b>Geometry</b>	<b>Pressure psia (MPa)</b>	<b>Mass Flux Mlbm/hr-ft<sup>2</sup> (kg/m<sup>2</sup>-s)</b>	<b>Inlet Subcooling °F (°C)</b>	<b>Max Exit Quality</b>
CISE	[[				
GE					
ASEA-713					
ASEA-813					
ASEA-513					]]

NEDO-33173 Supplement 1, Revision 0  
Non-Proprietary Information

The correlation statistics are presented in Table 1-2. The CISE, GE, and ASEA-713 test series form the development dataset for the correlation. The ASEA-813 and 513 test series represent the validation datasets (i.e., these were not used to develop the correlation).

**Table 1-2 Correlation Statistics for The Multi-Rod Database**

Dataset	Data Points (N <sub>i</sub> )	Ave. Error $\overline{\Delta\alpha} = \frac{1}{N_i} \sum_i (\alpha_m - \alpha_c)_i$	Std. Dev. <sup>2</sup> $\sigma = \sqrt{\frac{1}{N_i} \sum_i (\alpha_m - \alpha_c)_i^2 - (\overline{\Delta\alpha})^2}$
CISE	[[		
GE			
ASEA-713			
Development Set Subtotal <sup>3</sup>	.....	.....	.....
ASEA-813			
ASEA-513			
Validation Set Subtotal <sup>3</sup>	.....	.....	.....
Grand Total <sup>3</sup>			
95% Confidence Interval <sup>4</sup>			
95/95 Tolerance Interval <sup>5</sup>		]]	

<sup>2</sup> Note that the standard deviation quoted is for a population (“n” versus “n-1” degrees of freedom). This results in a small discrepancy in these values (compared to the grand total).

<sup>3</sup> The subtotals, as well as the grand totals for the datasets were combined using the formulas shown in Appendix E. The grand total includes both the development and validation sets (together).

<sup>4</sup> The 95% confidence interval for the mean is given by  $\bar{x} \pm \frac{z_{\alpha/2}}{\sqrt{n}} \sigma_p = \bar{x} \pm \frac{1.96}{\sqrt{n}} \sigma_p$  (large sample). The 95% confidence interval for  $\sigma$  is given by the range

$$\left[ \frac{(n-1)\sigma_p^2}{\chi_{\alpha/2, n-1}^2} \right]^{1/2} \text{ and } \left[ \frac{(n-1)\sigma_p^2}{\chi_{1-\alpha/2, n-1}^2} \right]^{1/2} = [[ \quad ]]$$

<sup>5</sup> Appendix E contains more detail concerning the tolerance interval.

### 1.3.1 Pressure Drop Based Data

At one point, a question was asked with regard to the 10x10 data presented in Section 2.0 as to whether the GE subset from Table 1-2 would be the most appropriate basis for comparison. The 10x10 data evaluation is based on pressure drop measurements. The GE 49-rod void measurements in the original database were also based on pressure drop measurements and evaluated as shown in Section 2.2.1. The agreement shown in Table 1-2 is excellent. Both the standard deviation and bias are very small. However, the GE 49-rod low flow dataset has unique attributes that should be considered in its interpretation:

- As stated in Section 3.1 of the report [9], the “General Electric data were used to specify the extreme low flow conditions of the correlation.” Given that the thermal-hydraulic conditions for the dataset were somewhat unique, and by virtue of the data’s application to develop the correlation, the agreement is quite good. Again, the correlation was designed to agree with these points.
- As mentioned in the first bullet point, the thermal-hydraulic conditions were somewhat unique. The 49-rod data were described in the report [9] as “very low” or “extreme low flow conditions.” Note that the range of flow rates considered in this test series was [[  
]] Mlbm/hr-ft<sup>2</sup>. The maximum flow rate from these tests is relatively low for BWR application and equivalent to the minimum value reported in Section 2.3 for the 10x10 comparisons. The majority of the 10x10 tests presented in Section 2.0 were conducted at higher flow rates.
- The GE 49-rod data were obtained from a special test configuration. [[

]]

- The tests were specially designed to measure void fraction. [[

]]

- The GE 49-rod tests were designed to minimize uncertainty. Comparing these tests to the CISE tests, which have the next lowest uncertainty value, the two

---

<sup>6</sup> The twelve measurements were used in conjunction with a weighting scheme to give the final (single) values reported for each run (Appendix F of NEDE-21565). This reduced the overall reported error.



uncertainties are statistically different at the 95% confidence level<sup>7</sup>. The small uncertainty in the GE 49-rod tests makes them unique relative to the rest of the Findlay-Dix database. Consequently, new tests would not be expected to match the 49-rod data uncertainties (either), unless similar steps are taken to minimize error. Noting that each run is an average of 12 measurements, scaling the reported standard deviation by  $\sqrt{12}$  gives [[ ]], which indicates that errors for individual observations were consistent (in magnitude) with the other reported values for the development data sets, as well as the 10x10 low flow uncertainties presented in Section 2.3.

In summary, the GE 49-rod tests were unique somewhat specialized for the purpose of correlation development. By itself, this particular dataset does not necessarily represent the expected uncertainty in bundle void fraction predictions based on the Findlay-Dix correlation. Table 1-3 gives a subset of low flow test cases from the ASEA test series (validation cases). The uncertainty in this data is comparable to the overall value presented in Table 1-2, as well as the value for the validation set subtotal.

**Table 1-3      ASEA-813, 713 Statistics – Comparisons of 8x8 Low Flow Void Fraction Measurements Versus Findlay-Dix Predictions – 1,000 psia,  $\Delta T_{\text{sub}} \sim 20$  °F, and Various Power Levels**

Test Series	Mass Flux (Mlbm/hr-ft <sup>2</sup> )	Test Run	No. of Points (Axial Planes)	$\overline{\Delta\alpha} = \frac{1}{n} \sum_{i=1}^n \Delta\alpha_i$	$\sigma = \sqrt{\frac{\sum_{i=1}^n (\Delta\alpha_i - \overline{\Delta\alpha})^2}{N}}$
813	[[				
713					
Grand Total <sup>8</sup>					]]

<sup>7</sup> Based on an  $F$ -test, where  $[[$

<sup>8</sup> Combined as shown in Appendix E.

#### 1.4 Application of the Findlay-Dix Correlation

The Findlay-Dix void correlation appears in several methodologies and NEDE-21565 is sometimes incorporated (directly) by reference in the subject Licensing Topical Report (LTR). Some of the key methods that utilize the correlation are summarized below in Table 1-4.

NEDE-21565 is an internal GE report. It has not been submitted for NRC review and approval. This reflects the philosophy that the void correlation should not be assessed in a generic, stand-alone sense. There is no independent, objective measure of “correctness” for the drift flux model. While smaller is generally better, in general, it is not possible to determine a priori if 5, 10, or 20% uncertainty in void fraction would be acceptable for a particular application. Consider the example of heat transfer coefficient correlations, many of which are notorious for 20% or more uncertainty relative to their databases. Despite relatively large uncertainties, these correlations can be successfully applied to produce temperature predictions for plant licensing evaluations. This fact is typically demonstrated through the qualification basis for the computer programs that support the methodologies. Each subject methodology must be assessed, not individual models, which is consistent with the steps defined in the CSAU methodology (NUREG/CR-5249). Uncertainties must be considered based on their impact on safety parameters. Key safety parameters are summarized in Table 1-4.

**Table 1-4 GE Methodologies That Employ the Findlay-Dix Correlation**

Methodology	Code & Application	Qualification
PANACEA NEDE-30130-P-A NEDE-24011-P-A	<p>PANACEA (or PANAC) is the steady state nuclear analysis code (3-D core simulator) for core design and reload licensing evaluations. It has nuclear and thermal hydraulic models suitable for predicting:</p> <ul style="list-style-type: none"> <li>• Depletion (fuel isotopic changes with exposure)</li> <li>• Power and flow distribution (radial and axial)</li> <li>• Total core thermal power</li> <li>• Reactivity changes</li> </ul> <p>PANAC is applied to predict margin to limits (SDM, MCPR, LHGR, etc.).</p>	<p>Plant operating and Post Irradiation Examination (PIE) data</p> <ul style="list-style-type: none"> <li>• Critical Eigenvalue (e.g., start up demonstrations)</li> <li>• TIP comparisons</li> <li>• Gamma scans</li> <li>• Radiochemical analyses of fuel segments</li> </ul>

NEDO-33173 Supplement 1, Revision 0  
Non-Proprietary Information

Methodology	Code & Application	Qualification
<p style="text-align: center;">ODYN NEDO-24154-A NEDE-24011-P-A</p>	<p>ODYN is a 1-D transient analysis code, used to predict system performance. It has models necessary to characterize the plant response to AOOs and ATWS scenarios:</p> <ul style="list-style-type: none"> <li>• Reactor core</li> <li>• Major system volumes, e.g., vessel, steam lines, recirculation piping, etc.</li> <li>• Valves, pumps, instruments, steam separators, etc.</li> <li>• Control system</li> </ul> <p>ODYN is applied to predict transient MCPR performance and peak vessel pressure. For MCPR calculations, boundary conditions from ODYN are used to drive a single, decoupled (hot) channel model (TASC).</p>	<p>Plant transient data and various separate effects tests</p> <ul style="list-style-type: none"> <li>• Peach Bottom Unit 2 turbine trip tests, which simulated void collapse, reactor protection system performance, and reactivity feedback</li> <li>• KKM turbine trip tests</li> <li>• Vallecitos boron mixing tests</li> <li>• BWR/6 loss of feedwater event</li> <li>• BWR/5 flow increase event</li> <li>• BWR/4 MG-set plant flow decrease event</li> </ul> <p>Comparisons include predictions versus plant instrument responses during transients: neutron flux, dome pressure, water level, core flow, and pump speeds.</p>
<p style="text-align: center;">TASC NEDC-32084P-A</p>	<p>TASC is a 1-D, single channel “hot bundle” transient model. In the ODYN based methodology, the hot channel is decoupled from the core (no feedback). TASC model includes:</p> <ul style="list-style-type: none"> <li>• One-dimensional transient heat conduction</li> <li>• A separated flow (mixture) model with Findlay-Dix drift flux</li> <li>• Multiple rod groups, pin power radial profile, hot channel gap conductance, etc.</li> <li>• Direct moderator heating</li> </ul> <p>TASC is applied to predict transient <math>\Delta</math>CPR in the limiting channel.</p>	<p>Comparisons to full-scale transient experiments (ATLAS and Stern Labs). The comparisons have been performed for 8x8, 9x9, and 10x10 fuel designs.</p> <ul style="list-style-type: none"> <li>• Simulated turbine trips, with and without recirculation pump trips</li> <li>• Simulated internal pump plant recirc trips</li> <li>• Predicted <math>\Delta</math>CPR magnitude and timing are compared to data</li> </ul> <p>Test section parameters such as power, pressure, and inlet flow were varied in the tests (i.e., the fuel reactivity feedback response was simulated).</p>

NEDO-33173 Supplement 1, Revision 0  
Non-Proprietary Information

Methodology	Code & Application	Qualification
ODYSY NEDC-32992P-A	<p>ODYSY is a linearized, small perturbation, frequency domain model of the reactor core and coolant circulation system. ODYSY is based on ODYN and employs a 1-D kinetics model.</p> <p>ODYSY can be applied to predict decay ratios for single channels, as well as reactor cores.</p>	<p>ODYSY has been qualified by comparisons to plant data (instability events and tests), including Vermont Yankee, LaSalle, Peach Bottom, Laguna Verde, KRB, Cofrentes, Caorso, Leibstadt, Nine Mile Point 2 and Perry.</p>
SAFER NEDE-30996P-A NEDE-23785-2-PA	<p>SAFER is an ECCS-LOCA model. The code contains the thermal-hydraulic and fuel related models necessary to evaluate LOCA scenarios:</p> <ul style="list-style-type: none"> <li>• Physical models for critical flow, post boiling transition heat transfer (including radiative heat transfer), etc.</li> <li>• Fuel rod thermal-mechanical (swelling and rupture)</li> <li>• Models for metal-water reaction</li> <li>• Counter Current Flow Limiting (CCFL) behavior</li> <li>• Vessel volumes for tracking liquid inventories</li> <li>• ECCS system models (ADS, low and high pressure injection systems, etc.)</li> </ul> <p>SAFER is applied to evaluate conformance with 10 CFR 50.46 criteria.</p>	<p>Separate effects tests and integral experiments, including</p> <ul style="list-style-type: none"> <li>• TLTA, ROSA-III, FIX-II, FLECHT and FIST-ABWR</li> <li>• Blow Down Heat Transfer (BDHT) tests and ATLAS</li> <li>• CCFL tests</li> </ul>

#### 1.4.1 Void Fraction Uncertainty Treatment

It is worth noting that the void fraction uncertainty quoted in NEDE-21565 is not directly “applied” to set limits or margins in the PANAC-ODYN based methods summarized in Table

1-4. [[

]] The discussion of power predictions brings up an interesting point, in that 10x10 gamma scans can be considered relevant for assessing the performance of models used in the simulator (all models, including the drift flux model, TGBLA models, etc.). Nodal comparisons can be used to examine the spatial (axial) accuracy, i.e., power predictions above the PLRs [22].

A void model uncertainty value was provided to the NRC staff as part of a supporting analysis for the application of OLYN. The statistical adders used in setting the Operating Limit MCPR (OLMCPR) are based on comparisons to the Peach Bottom turbine trip tests, but were supported by an additional confirmatory analytical perturbation analysis [10]. In this analysis, void fraction, as well as other important parameters, were varied and combined using the propagation of errors technique. [[

]]

This discussion is analogous to a previous response provided to a staff RAI, "Provide a summary of how the void-quality correlation uncertainties are accounted for in the model uncertainties for the codes and the analytical methodologies used to perform the licensing bases safety analyses." The staff evaluation of the GEH response is included in Appendix A of the safety evaluation for NEDC-33173P [2]:

*"GE notes that uncertainties for core power are generated for SLMCPR, LHGR, LOCA related limits are in general taken from in core power measurements in operating plants. These are developed by comparing code predictions to TIP response in operating plants. For OLMCPR, LHGR, and Stability limits power uncertainties are determined using overall uncertainties in the transient models that are generally developed from comparison to plant transients. Thus the uncertainty in these limits is not dependent directly on the uncertainty in the void prediction, but rather relies on uncertainties developed directly from power measurements or from overall transient prediction uncertainties. The NRC staff finds that void uncertainty levels therefore do not directly impact core power predictions for these cases."*

#### **1.4.2 Application to ECCS-LOCA Models**

Predictions of accident scenarios, like Loss of Coolant Accidents (LOCA), involve a wide range of conditions, i.e., a range of flow rates (including very low flow rates) and low pressures. The ECCS-LOCA model (SAFER) has specialized thermal-hydraulic models to predict mass, momentum, and energy transfer between regions of the reactor vessel.

- [[

- 

]]

In summary, with respect to void fraction, the SAFER methodology has specialized hydraulic models for application to ECCS-LOCA evaluations. The accuracy of the void correlation must be considered in the context of these models and their intended application. Furthermore, the SAFER-based application methodology considers Appendix K criteria, resulting in the incorporation of additional conservatisms. SAFER-based evaluations for licensing are not strictly best estimate.

Regarding the accuracy of the Findlay-Dix correlation as applied in SAFER, some of the low-pressure void fraction comparisons (e.g., 15 to 150 psia) have relatively high uncertainties, as shown in Table 5-2 of NEDE-21565. However, the SAFER application of the bubble rise and drift flux models for two-phase level prediction is supported by qualification against experimental data. Section 6 of NEDE-30996P-A (see Table 1-4) includes comparisons against data from the TLTA, ROSA-III, FIX-II, and FIST-ABWR test series. These are integral tests that demonstrate SAFER's accuracy in predicting system depressurization behavior and liquid inventories.

The Findlay-Dix void correlation is applied to conditions where counter-current flow may exist, but not in the manner described in NEDE-21565<sup>9</sup>. The SAFER code is applied for ECCS-LOCA evaluations where counter-current flow conditions are likely. SAFER considers counter-current flow phenomena in order to perform the mass, energy, and momentum balances between regions inside the vessel. To this end, SAFER employs the Modified Wallis correlation to model Counter-Current Flow Limiting (CCFL) behavior at specific locations (geometrically restricted areas). Once the mass flow rates at the region boundaries are established, the Findlay-Dix or bubble rise models may be applied within the region as described above. More discussion has been provided in the newest revision of NEDC-32950 (MFN 07-406).

---

<sup>9</sup> NEDE-21565 was provided to the staff in order to support Vermont Yankee's power uprate application and the review of NEDC-33173P. The NEDE-21565 report is an internal document. While it contains an accurate description of the void correlation and its associated database, the suggestions for further investigation contained therein (e.g., applying Findlay-Dix to counter-current flow) are outdated.

### 1.4.3 Application to Transient Models

ODYN is applied to predict BWR system transient performance. ODYN utilizes the Findlay-Dix correlation and has been qualified against plant transient data (Table 1-4). Confirmatory uncertainty evaluations were also performed as described under Section 1.4.1. Boundary conditions from ODYN calculations are typically used to drive a single-channel calculation in order to determine the limiting bundle's MCPR response.

Both ODYN and TASC employ the (same) Findlay-Dix correlation using a separated flow (mixture) model. The TASC code is applied to predict bundle transient performance (i.e., a single “hot” or limiting channel). TASC has been compared to full-scale transient tests for 10x10 fuel products. The qualification comparisons show that TASC accurately predicts bundle transient performance.

#### 1.4.3.1 Void Coefficient and Expected Sensitivities (Trends) for EPU/MELLLA+

Generally, in BWR fuel, increases in void fraction result in an undermoderated state and drive a reduction in neutron multiplication (i.e., decreased reactivity). Conversely, decreases in void fraction tend to increase neutron multiplication. This relationship between void fraction and reactivity is the dominant feedback mechanism in the BWR core. As a convenience, this behavior is often characterized and discussed in terms of a dynamic void coefficient. However, in PANAC-ODYN based methods, void coefficients are not explicitly calculated. Reactivity changes are determined directly from nuclear cross section information as a function of the calculated thermal-hydraulic state.

Pressurization events generally tend to limit BWR operation. Pressurization events inject positive reactivity due to void collapse, which increases power. Depressurization transients tend to reduce reactor power and are typically non-limiting.

The void coefficient increases (i.e., becomes more negative) with increasing void fraction. However, the rate of void production with increased power tends to decrease and offset this effect. Void production as a function of power is non-linear, which can be seen by plotting void fraction in the void versus quality plane. Figure 1-1 shows void fraction values predicted using the Findlay-Dix correlation under low flow, high power conditions (1,000 psia, 20 Btu/lbm subcooling, and ~0.55 Mlbm/hr-ft<sup>2</sup>). Recognizing that  $\Delta X \propto \Delta Power$ , the net void reactivity feedback due to a power change is given by Equation (1.7).

$$\frac{\Delta k}{k} = \underbrace{-\frac{1}{k} \frac{\partial k}{\partial \alpha}}_{\text{Void Coefficient}} \Delta \alpha \approx -\frac{1}{k} \frac{\partial k}{\partial \alpha} \left( \frac{\partial \alpha}{\partial X} \right) \Delta X \quad (1.7)$$

The  $\Delta k$  effectively diminishes for energy addition at high void fraction values, as depicted by Figure 1-1 (below) and Figure 2-2 in NEDC-33173P. The derivative  $\partial \alpha / \partial X$  varies with quality and becomes very small at high void fractions. In other words, reduced liquid in the fuel lattice equates to reduced reactivity ( $\Delta k \rightarrow \sim 0$  as  $\alpha \rightarrow 1.0$ ). This relationship (alone) would lead one to believe that a core with a higher (initial) void content would generally tend to have a milder

transient response than the same core with lower void content, which would help explain why calculated OLMCPR values have not been observed to radically change between pre-EPU and post-EPU designs. The characteristic change in void fraction with power  $\partial\alpha/\partial X$  acts like a “gain” factor and works against  $\partial k/\partial\alpha$  at high void values.

[[

]]

**Figure 1-1 Void Quality Relation [12]**

During a pressurization event (transient), many changes occur in a BWR bundle. Computer programs applied to predict such an event are modeling a fairly complex set of coupled phenomena, i.e., the void collapse, nuclear power feedback, heat conduction and transport across the fuel-cladding gap, and the subsequent (thermal-hydraulic) density wave that propagates through the channel. The void-quality relation as depicted in Figure 1-1 is still conceptually valid (in terms of the characteristic change in slope that is shown), but for this situation it would be more accurate to present a family of curves corresponding to the different pressures or a 3-D surface plot. Chen and Andersen have provided a detailed discussion of the relevant phenomena [11] for fast transients.

All core designs change from cycle to cycle, due to the efforts expended to optimize the designs. So comparisons of pre and post-EPU cores are confounded with other changes made for reload considerations. Furthermore, the system characteristics (pre versus post-EPU) may change due



to equipment upgrades necessary to support EPU or expanded operating domains. Regardless, core transient results (e.g., peak pressure) have been shown to be relatively insensitive to the void coefficient [12].

## **1.5 Fuel Thermal-Hydraulic Testing**

In order to comply with licensing commitments under GESTAR II [13],[14], the introduction of new fuel products involves comprehensive thermal-hydraulic testing for both critical power and pressure drop performance. These tests are performed using full-scale, electrically heated replicas of BWR fuel designs under thermal-hydraulic conditions (pressure, mass flux, and inlet subcooling) expected in service. Both steady state (critical power and pressure drop) and transient tests (critical power) are performed.

In critical power tests, the fuel assembly power level is increased in a quasi-steady manner for a given set of thermal hydraulic conditions to drive boiling transition in an instrumented bundle. Various rod-to-rod peaking patterns are tested at different conditions with the objective of experimentally examining each unique lattice position. This allows the lattice positions to be characterized, including geometry dependencies, for the purpose of the critical power correlation. The peaking patterns, combined with a test matrix of varied thermal hydraulic conditions (pressure, flow rate, and inlet subcooling), typically results in large database of experimental points for each fuel product. These points will be at very high void fractions and steam quality, characteristic of conditions at incipient boiling transition.

One or more peaking patterns developed for critical power testing will be selected for pressure drop testing. In these tests, thermal hydraulic conditions (mainly flow and power level, which changes steam quality) are varied. The test assemblies are instrumented with pressure taps so that the pressure profile data can be captured. This data can be used to either empirically develop, or experimentally confirm, spacer loss coefficients. Note that the methods used to determine frictional and acceleration losses are part of a set that includes the void correlation (elevation head loss), so only the spacer contributions need to be individually determined for new designs. Spacer losses must account for their unique geometry features and can be developed based on scaling analyses (e.g., analytic approaches [15]), then confirmed experimentally.

### **1.5.1 New Design Features**

New design features have been incorporated into BWR fuel bundles since the development of the Findlay-Dix correlation. Advanced fuel designs have been developed using smaller fuel rod diameters (larger array sizes), multiple and large diameter water rods, and spacers specially developed to optimize critical power and pressure drop performance. Note that spacers introduce a local perturbation to the flow field, but generally do not impact average void fraction predictions. However, some of these newer design features result in relatively small changes in flow area and characteristic length (hydraulic diameter).

Partial Length Rods (PLRs) are a relatively new design feature that has been incorporated into GNF fuel products. PLRs are essentially just shorter versions of the standard (full-length) fuel rod design. The presence of the PLR within the fuel channel creates a change in the (1-D) axial flow area. In addition to the local effect or perturbation, the in-channel bulk flow experiences a very slight deceleration and pressure change as a result of the area change. Note that the GNF2 product line contains two sets of PLRs (two different heights), which results in two flow area changes.

Reference [16] contains a discussion of experiments that were conducted to examine the impact of PLRs on void fractions. The experiments considered 4x4 and 8x8 assemblies, both with and without PLRs present. This approach allowed comparisons of experiments (i.e., data versus data) to examine the impact of the perturbation introduced by PLRs. The studies found that PLRs have a very small impact on void fraction. The observed differences were within the measurement uncertainty of the data.

## **1.6 Subchannel Versus Planar Average Void Fraction**

In reactor simulation, the void correlation is applied to fuel channels to determine the one-dimensional void fraction (i.e., the planar average void fraction as a function of elevation). The void fraction information is essentially used to “look up” cross section data based on infinite lattice calculations, which are typically performed based on a single void value. This common technique used in (nodal) core simulators ignores radial void fraction variations within bundles (which would be expected to be induced by variation in rod-to-rod local peaking). Studies have been conducted to examine this effect [16], [17]. Both the study in NEDC-32601P-A [16] and Ama’s results [17] are well described and illustrate that local void fractions are expected to have a slight flattening effect on the pin power distribution due to local feedback. The simplified lattice physics treatment discussed here slightly overestimates the peak pin power.

Insertion of a control blade will suppress bundle power and “skew” the pin-wise power distribution (increasing away from the blade). The resulting power feedback impacts the channel void distribution. The lattice physics code TGBLA has the capability to utilize a non-uniform void distribution in order to capture this effect [18]. The TGBLA model incorporates the local void effect on pin peaking directly into the nuclear calculations that produce data for downstream analyses. In the PANAC-ODYN based methodology, TGBLA output (e.g., nuclear cross sections and local peaking factors) essentially forms a multi-dimensional library of parameters as a function of average void fraction, state (controlled or uncontrolled), exposure, and lattice position (as applicable). The peaking data from this library is used in downstream analyses to establish cycle specific design margins to critical power and Linear Heat Generation Rate (LHGR) limits. Note that the SAFER based accident analyses are not tied to the TGBLA calculation in this manner, e.g., LOCA evaluations are typically performed in a cycle independent manner for a particular fuel type.

Critical power predictions consider pin-by-pin peaking through the GEXL methodology, which is both developed and validated based on full-scale tests. These tests include both steady state

and transient thermal-hydraulic experiments (Section 1.5). In order to translate between the critical power database and the designs developed for operating reactors, the TGBLA based power distributions are used as input into the GEXL methodology. This implies an equilibrium or quasi-steady assumption, since instantaneous void feedback on local rod powers is not treated. However, analytic studies considering fully coupled problems confirm that this approach is also adequate for rapid transients [11], [19].

Considering local peaking further, it is worth noting that BWR fuel bundles are usually designed considering a line of symmetry. Typically, rod enrichments are evenly distributed with respect to the line of symmetry. This promotes symmetric (not “skewed”) pin-wise radial peaking patterns in the uncontrolled state. The ASEA-813 test bundle simulated a “skewed” power radial distribution, but independent of the power suppression that would be expected with an inserted control blade. The ASEA-813 tests were part of the Findlay-Dix validation set and included void fractions in excess of 90%.

Also note that the previous section (Section 1.2) contained some relevant comments concerning local effects and the distribution parameter. The one dimensional drift flux formulation essentially loses local information through the averaging process. In application to fuel calculations, the objective of the 1-D correlation is to properly calculate the average void fraction given the nodal (“global slip”) conditions within the channel. However, in order to properly consider this effect, the approach taken with TGBLA is to re-introduce local void information into the lattice calculation through an empirical correlation. The model is applied in a manner that provides an adjustment over the range where sensitivity is expected.

### **1.6.1 In-Channel Void Distribution Model**

TGBLA06 has the capability to calculate the impact of non-uniform void distributions on pin-by-pin power and lattice reactivity. [[

(1.8)

]]

**Table 1-5      Values of Edge Rod Factors  $k(x,y)$  Used in Equation (1.8)<sup>10</sup> for Controlled Lattices**

(x,y)	(x,1)	(x,2)	(x,3)	(x,4)	(x,5)
(1,y)	[[				
(2,y)					
(3,y)					
(4,y)					
(5,y)					]]

[[

(1.9)

(1.10)

(1.11)

(1.12)

(1.13)

---

<sup>10</sup> [[ ]]

]]

---

<sup>11</sup> Geometry characteristics (length scales) associated with the databases supporting the COBRAG constitutive relations can be inferred to limit maximum and minimum subchannel sizes, but not their number. Note that any limitations of this nature could be extended by validation against experimental data.

<sup>12</sup> A 10x10 lattice with 3.61% average enrichment, 8 Gadolinia rods at 5%, and no vanished rods.

**Table 1-6 Controlled Lattice Void Distribution Based on TGBLA**

(x,y)	(x,1)	(x,2)	(x,3)	(x,4)	(x,5)	(x,6)	(x,7)	(x,8)	(x,9)	(x,10)
(1,y)	[[									
(2,y)										
(3,y)										
(4,y)										
(5,y)										
(6,y)										
(7,y)										
(8,y)										
(9,y)										
(10,y)										]]

**Table 1-7 Controlled Lattice Void Distribution Based on COBRAG**

(x,y)	(x,1)	(x,2)	(x,3)	(x,4)	(x,5)	(x,6)	(x,7)	(x,8)	(x,9)	(x,10)
(1,y)	[[									
(2,y)										
(3,y)										
(4,y)										
(5,y)										
(6,y)										
(7,y)										
(8,y)										
(9,y)										
(10,y)										]]

**Table 1-8 Uncontrolled Lattice Void Distribution Based on TGBLA**

(x,y)	(x,1)	(x,2)	(x,3)	(x,4)	(x,5)	(x,6)	(x,7)	(x,8)	(x,9)	(x,10)
(1,y)	[[									
(2,y)										
(3,y)										
(4,y)										
(5,y)										
(6,y)										
(7,y)										
(8,y)										
(9,y)										
(10,y)										]]

**Table 1-9 Uncontrolled Lattice Void Distribution Based on COBRAG**

(x,y)	(x,1)	(x,2)	(x,3)	(x,4)	(x,5)	(x,6)	(x,7)	(x,8)	(x,9)	(x,10)
(1,y)	[[									
(2,y)										
(3,y)										
(4,y)										
(5,y)										
(6,y)										
(7,y)										
(8,y)										
(9,y)										
(10,y)										]]

[[

]]

---

<sup>13</sup> Defining the error as  $Err = (\alpha_T - \alpha_C)$  for the values shown in the tables.



## 2.0 COMPARISONS TO THERMAL-HYDRAULIC DATA

### 2.1 Pressure Drop Bias and Uncertainty

#### 2.1.1 Measurement Bias and Uncertainty

A measured pressure drop ( $\Delta P$ ) for a particular test run can be expressed with error terms. Any given measurement may contain a systematic bias, as well as a contribution due to random error ( $\pm \varepsilon$ ). However, in this analysis, the measurement bias is assumed to be zero.

$$\Delta P_{Tot, Meas} = \Delta P_{Tot} + \cancel{\delta P_{Meas}} \pm \varepsilon_{Meas} \quad (2.1)$$

Measurement bias is minimized (eliminated) by good experimental practices (e.g., calibration of pressure gages, etc.). So the observed  $\Delta P$  is taken as an actual pressure drop with a random error component.

#### 2.1.2 Calculational Bias and Uncertainty

##### 2.1.2.1 Calculated Pressure Drop Average Error or Bias

A pressure drop calculation can also be considered to include an error or bias ( $\delta P$ ) term. Correlation accuracy could (potentially) be a source of error, as well as approximations or assumptions inherent in the method and numerical errors (truncation and round-off). Calculated errors are constant in the sense that bias is reproducible for a particular case or set of computer program inputs. However, the magnitude of the error may change for different conditions (cases) and it may be positive or negative. For a particular set of boundary conditions, geometry, etc., (i.e., for a particular instance or calculation) the pressure drop can be written

$$\Delta P_{Tot, Calc} = \sum_i \sum_j (\Delta P_{i,j} + \delta P_{i,j}) = \Delta P_{Tot} + \sum_i \delta P_{Calc,i} \quad (2.2)$$

Equation (2.2) is shown in a form consistent with most nodal calculation methods in the sense that pressure loss terms may be summed over each axial node “j” for each type of loss “i” (acceleration, friction, etc.). Equation (2.2) essentially states that the calculated pressure drop is composed of an actual  $\Delta P$  value or result that would be real or observable (in an experiment) plus a residual error term attributable to calculation inaccuracy.

The calculated steady state pressure drop can be expressed in terms of its components. Expanding Equation (2.2) for steady-state conditions and considering totals for the channel (of each loss type “i”)

$$\Delta P_{Tot, Calc} = \Delta P_{Elev} + \Delta P_{Exp/Con} + \Delta P_{Fric} + \Delta P_{Loc} + \Delta P_{Acc} + \sum_i \delta P_i \quad (2.3)$$

The total steady state pressure drop consists of components due to elevation, wall friction, local losses, acceleration, and sudden expansions or contractions (another form of acceleration loss).

The pressure loss due to expansion / contraction is relatively small in a BWR fuel channel and may be neglected in this analysis

$$\delta P_{Exp/Cont} \approx 0 \quad (2.4)$$

There may be a substantial expansion at the exit of an actual BWR bundle (where the rodded region ends). However, this is not true of the test section, where the region above the bundle exit contains test apparatus, i.e., the electrically heated test rods typically extend into this region. The upper pressure tap is still within a rodded region, where the area change is less dramatic than the bundle exit.

As presented in Appendix C, the frictional loss terms shown in Equation (2.3) are calculated based on flow rate, steam quality, and liquid/steam properties (e.g., density). For the purposes of this analysis, all of the calculational bias can be assumed to be due to errors in the void fraction

$$\delta P_{Fric} = \delta P_{Loc} = \delta P_{Acc} = 0 \quad (2.5)$$

Other potential sources of calculational error (e.g., model uncertainties or geometry approximations) are ignored in the sense that they are not treated explicitly. However, if other potential sources of error are present, then their contribution will be attributed to the remaining term.

For low flow experiments, Equation (2.5) is a good approximation. Both physically and for the calculation, the acceleration, local losses, and frictional contributions to the overall pressure drop are relatively small. In other words,

$$\underbrace{\left| \frac{1}{n} \sum_i^n \delta P_i^{Elev} \right|}_{\Delta P \propto \alpha} \geq \underbrace{\left| \frac{1}{n} \sum_i^n (\delta P_i^{Acc} + \delta P_i^{Fric} + \delta P_i^{Loc}) \right|}_{\Delta P \propto \text{acceleration, friction, etc.}} \quad (2.6)$$

Under these assumptions, the error term ( $\delta P$ ) in Equation (2.3) reduces to a single term related to elevation head, as opposed to a summation of various source terms. The residual error (i.e., the difference between calculated and measured pressure drop) can be written

$$\delta P \approx \delta P_{Elev} \approx \Delta P_{Tot,Calc} - \Delta P_{Tot,Meas} \pm \varepsilon_{Meas} \quad (2.7)$$

This is Equation (2.3) minus (2.1). Again, any systematic error has been assumed to be due to a single source, which is the calculated void fraction. This can also be thought of as “assigning” all of the error to the void fraction calculation.

Equation (2.7) represents a comparison for an instance or single example. Examining the bias over an ensemble or collection will give an average bias. The average bias will represent a general tendency to over or under-predict  $\Delta P$  (depending on the value). This value will also have some amount of uncertainty, or inherent variation.

### 2.1.2.2 Calculated Pressure Drop Uncertainty

[[

]] Also, in the pressure drop experiments of interest, there is no power feedback from void fraction changes. Therefore, the calculated void fraction does not influence the axial power and predicted quality profile through the bundle.

[[

]] (2.8)

The consequence of this observation is that errors in calculated void fraction do not have an impact on calculated pressure drop uncertainty, except through the elevation head term. In terms of propagation of errors,

$$\sigma_x^2 = \left( \frac{\partial x}{\partial u} \right)^2 \sigma_u^2 + \left( \frac{\partial x}{\partial v} \right)^2 \sigma_v^2 + \dots + \left( \frac{\partial x}{\partial z} \right)^2 \sigma_z^2 \quad (2.9)$$

the sensitivity coefficients (i.e., the derivatives in Equation (2.8)) are zero.

$$\sigma_{\Delta P_{calc}}^2 = \underbrace{\left( \frac{\partial \Delta P}{\partial \alpha} \right)^2 \sigma_\alpha^2}_{\text{elevation head}} + \underbrace{\left( \frac{\partial \Delta P}{\partial X} \right)^2 \sigma_X^2}_{\text{flow quality}} + \dots + \underbrace{\sum_i \left( \frac{\partial \Delta P}{\partial x_i} \right)^2 \sigma_{x_i}^2}_{\text{other terms, e.g., model parameters, flow, fluid properties, etc.}} \quad (2.10)$$

The design methods (“Method B”) used for pressure drop calculations in licensing applications are typically discussed in topical reports (e.g., Table 1-4). For convenience, the analytic expressions for the terms in Equation (2.3), i.e., the formulas for the pressure drop components, are presented in Appendix C.

## 2.2 Void Fraction Bias and Uncertainty

### 2.2.1 Void Fraction Average Error or Bias

The two-phase elevation pressure drop is given by

$$\Delta P_{Elev, Calc} = \frac{\bar{\rho} g \Delta z}{g_c} = \frac{g \Delta z}{g_c} [\bar{\alpha} \rho_g + (1 - \bar{\alpha}) \rho_{liq}] \cong \frac{g \Delta z}{g_c} [\bar{\alpha} \rho_g + (1 - \bar{\alpha}) \rho_f] \quad (2.11)$$

Equation (2.11) is written in terms of the total two-phase elevation pressure drop, so the void fraction ( $\alpha$ ) is shown with a bar to indicate that this is an average over the volume being modeled. In this sense, the void fraction value represents the relative volumes of fluid and vapor over the length ( $\Delta z$ ) between (simulated) pressure taps.

Equation (2.11) can be expanded to include error terms. Since the error in the calculated elevation head is assumed to be due to the void fraction calculation (i.e., one-to-one correspondence), a simple relationship can be determined. Introducing a small perturbation by substituting  $\bar{\alpha} + \delta\bar{\alpha}$  for void fraction and  $\Delta P + \delta P$  for pressure drop in Equation (2.11) gives

$$\Delta P_{Elev,Calc} + \delta P = \frac{g\Delta z}{g_c} \{ (\bar{\alpha} + \delta\bar{\alpha})\rho_g + [1 - (\bar{\alpha} + \delta\bar{\alpha})]\rho_f \} \quad (2.12)$$

Rearranging terms gives

$$\Delta P_{Elev,Calc} + \delta P = \frac{g\Delta z}{g_c} [\bar{\alpha}\rho_g + (1 - \bar{\alpha})\rho_f] + \frac{g\Delta z}{g_c} (\rho_g - \rho_f) \delta\bar{\alpha} \quad (2.13)$$

Comparing Equation (2.13) to (2.11), or subtracting, gives an expression relating the void error to a pressure drop error

$$\delta\bar{\alpha} = \frac{g_c \delta P}{g\Delta z (\rho_g - \rho_f)} \quad (2.14)$$

Substituting Equation (2.7) for  $\delta P$  gives an expression in terms of the calculated minus measured pressure drop

$$\delta\bar{\alpha} = \frac{g_c (\Delta P_{Tot,Calc} - \Delta P_{Tot,Meas} \pm \varepsilon_{Meas})}{g\Delta z (\rho_g - \rho_f)} \quad (2.15)$$

Under these assumptions, the error in the predicted (average) void fraction in a bundle is only dependent on the difference between the calculated and measured pressure drop, the elevation difference between pressure taps, the saturated liquid and vapor densities, and a contribution from a random measurement error. Taking an average over a collection of “N” observation-prediction pairs gives an expression for the mean error (bias) in void fraction

$$\overline{\delta\bar{\alpha}} = \frac{1}{N} \sum_i \delta\bar{\alpha}_i = \frac{g_c}{g\Delta z (\rho_g - \rho_f)} \frac{1}{N} \sum_i (\Delta P_{Tot,Calc,i} - \Delta P_{Tot,Meas,i} \pm \varepsilon_i) \quad (2.16)$$

If the measurement error is normally distributed, as the sample size increases, the sum of the errors decreases and the average becomes a better estimate of the mean.

$$\overline{\delta\bar{\alpha}} = \frac{1}{N} \sum_i \delta\bar{\alpha}_i = \frac{g_c (\overline{\Delta P_{Tot,Calc} - \Delta P_{Tot,Meas}})}{g\Delta z (\rho_g - \rho_f)} \quad (2.17)$$

In the right-hand side of Equation (2.17), the random error term has been dropped, i.e.,  $\frac{1}{N} \sum \pm \varepsilon_i \rightarrow 0$  as N becomes large (i.e., positive and negative errors are equally likely). Note that the RMS of the  $\varepsilon_i$  is a non-zero value; this essentially represents measurement uncertainty ( $\sigma_{Meas}$ ).

### 2.2.2 Void Fraction Uncertainty

Equation (2.7) gives the error residual in terms of calculational and measurement error. Similarly, the pressure drop uncertainty can be represented as a sum of variances from the two independent sources

$$\sigma_{\delta P}^2 = \sigma_{Calc}^2 + \sigma_{Meas}^2 \quad (2.18)$$

The left hand side of Equation (2.18) can be directly obtained from the calculated minus measured pressure drops, i.e., a calculation of the standard deviation based on the calculation-measurement pairs. Letting  $x = \Delta P_{Calc} - \Delta P_{Meas}$ , the uncertainty in “x” can be estimated as the standard deviation of a sample

$$\sigma_{\delta P}^2 \approx s^2 = \frac{1}{N-1} \sum_i^N (x_i - \bar{x})^2 \quad (2.19)$$

The measurement uncertainty may be obtained from experimental information. Once two of the three quantities in Equation (2.18) are established, the remaining uncertainty can be determined.

The terms in (2.18) can be evaluated and combined using the propagation of errors technique. In order to apply this technique, expressions for sensitivity coefficients (derivatives) are necessary. Using the assumptions employed to derive Equations (2.10) and (2.15), it is only necessary to evaluate a term for the elevation pressure loss in order to evaluate the calculational uncertainty. Substituting Equation (2.10) for calculational error

$$\sigma_{\delta P}^2 = \left( \frac{\partial(\Delta P)}{\partial \bar{\alpha}} \right)^2 \sigma_{\bar{\alpha}}^2 + \sigma_{Meas}^2 \quad (2.20)$$

The sensitivity coefficient can be obtained by differentiating Equation (2.11). Substituting and rearranging gives

$$\sigma_{\bar{\alpha}} = \pm \sqrt{\frac{\sigma_{\delta P}^2 - \sigma_{Meas}^2}{\left( \frac{\partial(\Delta P)}{\partial \bar{\alpha}} \right)^2}} = \pm \sqrt{\frac{\sigma_{\delta P}^2 - \sigma_{Meas}^2}{\left[ \frac{g \Delta z}{g_c} (\rho_g - \rho_f) \right]^2}} = \pm \frac{g_c \sqrt{\sigma_{\delta P}^2 - \sigma_{Meas}^2}}{g \Delta z (\rho_g - \rho_f)} \quad (2.21)$$

This approach for treating uncertainty produces a similar result (in terms of form) to Equation (2.14), since consistent assumptions have been applied. However, in order to solve (2.21), an expression or estimate for the measurement uncertainty is necessary. Otherwise, the measurement uncertainty can conservatively be taken as zero.

Note that Equations (2.18) and (2.9) represent the case of independent (uncorrelated) errors. The predicted versus measured results are well correlated. However, the existence of correlation between two variables does not imply causality. For the most part, the experimental  $\Delta P$  values are not used as inputs to the pressure drop calculations. [[

]] In other words, the single-phase spacer loss coefficients were derived to best match a subset of the measured data, so there is a possibility of correlated errors between these points that is ignored. In contrast, the GNF2 spacer loss coefficients were projected from an area scaling analysis applied to the GE14 spacer geometry. The GNF2 loss coefficients were determined a priori and the  $\Delta P$  testing was confirmatory. Furthermore, the Findlay-Dix void prediction (i.e., the assumed source of calculational error) is based on a completely different experimental database, independent of the 10x10  $\Delta P$  measurements. For these reasons, the errors are treated as uncorrelated.

### 2.2.3 Assumption Summary

In the preceding sections, various assumptions are discussed. The assumptions used to derive the expressions in this section include:

- Steady state conditions are assumed
- All of the calculated error is assigned to the void fraction calculation, regardless of the actual source
- Experimental error is random (only) and no bias is assumed
- Calculated  $\Delta P$  error due to void fraction error is independent of other error sources. The thermal-hydraulic tests do not have void feedback, which affects calculated power, flow quality, pressure drop and flow. Also, loss coefficients, which establish the calculated  $\Delta P$  are determined either based on a subset of data or completely independently of the data. Furthermore, under low flow conditions, contributions from local losses, friction, and acceleration are minimized.
- Losses due to sudden expansion (e.g., above the PLR within the bundle) are ignored (Equation (2.4)) in the propagation of error analysis
- The expression used in this analysis for the elevation pressure drop considers the fluid properties at saturation conditions (i.e.,  $\rho_f \approx \rho_{liq}$ )
- Errors associated with the calculational model (e.g., differences between the as-modeled geometry and the experiment) are assumed to be small and are ignored

An additional assumptions are made in the analysis:

- Fluid properties are evaluated at a single system pressure (i.e., the change in saturated liquid and vapor densities due to the pressure drop within the bundle is ignored). In addition, the system pressure measurement in the experiments

[[

]] This slight variation is ignored in the void error estimate. However, the computer evaluations use the measured system pressure (and subcooling) values that were reported for each test run.

- Only co-current upflow is considered

## 2.3 Low Flow Rate Test Results

Figure 2-1 shows a subset of GE14  $\Delta P$  test data. The figure shows that the total pressure drop for the  $< 3$  MWt,  $< 0.3$  Mlbm/hr-ft<sup>2</sup> data actually dips below the 0 MWt (single-phase) pressure drop data. In these cases, friction is relatively low and introducing voids reduces the average water density, which reduces  $\Delta P_{Elev}$  and causes a net reduction in the total pressure drop relative to the single-phase (0 MWt) case. This subset of 6 points has the lowest frictional pressure loss (i.e., the components due to friction, local, and acceleration losses, or  $\Delta P \propto G^2$ ) of the GE14 test set. This illustrates that for these cases, properly calculating the contribution from elevation head is very important for accurately predicting the total  $\Delta P$ .

In general, under low flow conditions, both the “integral slip” ( $C_o$ ) and “local slip” ( $v_{gj}$ ) contributions to void fraction are important. So the low flow cases provide a good test for all of the Findlay-Dix correlating functions. At higher flow rates, void fraction tends to more strongly depend on  $C_o$  (see Appendix B, Equation (B.18)).

[[

]]

**Figure 2-1 GE14  $\Delta P$  Versus Mass Flux For the 0 to 3 MWt Test Runs**

Table 2-1, Table 2-2, Table 2-3, and Table 2-4 present low flow pressure drop data for three (3) GE product lines. All of these fuel designs are based on 10x10 lattices.

The definitions of the column headings in the table are as follows:

- Test run and conditions – these columns contain the assembly identifier, test run number, assembly power, and hydraulic conditions.
- DPX – the “X” is a number corresponding to the differential pressure transducer in the test facility. The transducers were configured to measure axial segments of the test assemblies. The height corresponding to the segment is given in inches.
- Top Quality – the one-dimensional average flow quality at the top of the axial segment, as determined by a steady state heat balance (see Appendix B).
- $\delta P$  – given by Equation (2.7).
- $\delta \alpha$  – determined from  $\delta P$  using the method outlined in Section 2.2.1. Note that the overbar indicating an average has been dropped (for convenience).



NEDO-33173 Supplement 1, Revision 0  
Non-Proprietary Information

Two figures (Figure 2-2 and Figure 2-3) follow the tables. These are graphical representations of the tabular data. Figure 2-4 shows an example of calculated axial void profiles for one of the test series.

<sup>15</sup> These calculated values are unadjusted for ATLAS pressure drop measurement error [

Test Run and Conditions						DP2 (2 - 150 inches)			DP9 (84 - 102 inches)			DP4 (102 - 150 inches)		
STA	Run	Power (MW/t)	Mass Flux (Milbm / hr-ft <sup>2</sup> )	P (psia)	T <sub>in</sub> (°F)	Top Quality	δP (psid)	Calc δα	Top Quality	δP (psid)	Calc δα	Top Quality	δP (psid)	Calc δα
[[														
						Average								
						Standard Deviation						]]		

## Comparisons To Thermal-Hydraulic Data



[[

]]

**Figure 2-2      Calculated  $\delta\alpha$  Versus Quality By Bundle Segment ( $\Delta z$ )**

[[

]]

**Figure 2-3      Calculated  $\delta\alpha$  Versus Quality (from Figure 2-2) By Fuel Type**

[[

]]

**Figure 2-4 Example Calculated Void Profiles for GE14 Low Flow Tests**

### **2.3.1 GE12 Low Flow Tests**

The results for two test assemblies are presented. Three sets of axial segments are given for each run: full length, the lower test section up to 118 inches (which contains the PLR transition at [[ ]]), and the uppermost test section (high void fraction region).

Test runs 322 and 570 were at relatively high power levels (4 MWt), especially given the low mass flow rates. The total measured pressure drop for these cases is less than the comparable single-phase (0 MWt) case, so the void contribution to pressure drop is important. However, the friction, local, and acceleration losses are relatively high. These cases have significant acceleration and relatively high velocities, especially in the upper elevations of the bundle. These cases could be excluded from the set on this basis. The frictional losses are about 65% of the total, where the elevation loss makes up the remaining 35%.

If the 4 MWt cases are included, the data sets are normal, with the exception of the 118 to 152 inch segment data. However, excluding the 4 MWt cases (consistent with the discussion above) for the purpose of comparing data, the residuals ( $\delta\alpha$ ) for the various axial segments are all normally distributed. Performing comparisons with the normal data, the 4 to 118 inch set is



statistically different relative to the other two sets, which is consistent with the transducer problem noted in the test records. The uncertainty for this set is significantly larger than the other sets. The 2 to 150 inch and 118 to 153 data sets (which were not directly affected by the transducer problem) are not different (means or variances) at the 95% confidence level.

### 2.3.2 GE14 Low Flow Tests

Three sets of axial segments are presented: full length, a mid-height test section from 84 to 102 inches, and the uppermost test section from 102 inches to the end of the heated length (high void fraction region). The end of the heated length of the GE14 PLR is at [[ ]]. The physical end of the PLR is at [[ ]] (flow area transition).

The residuals ( $\delta\alpha$ ) for the various axial segments are normally distributed. The three data sets are not different (means or variances) at the 95% confidence level. The data from upper segment with the highest void fractions, the segment straddling the PLRs, and the full-length section are not significantly different.

### 2.3.3 GNF2 Low Flow Tests

#### 2.3.3.1 Inlet Peaked Data

Three sets of axial segments are presented: full length, a mid-height test section from 102 to 118 inches, and the uppermost test section from 102 inches to the end of the heated length (highest void fraction region). [[ ]].

The residuals ( $\delta\alpha$ ) for the mid-height axial segments are normally distributed. The residuals for the full-length and uppermost sections are slightly non-normal ( $P = 0.039$  and  $0.042$ , respectively, calculated with  $\alpha = 0.05$ ). Ignoring this and comparing the three data sets, they are not different (means or variances) at the 95% confidence level.

#### 2.3.3.2 Cosine Data

Equipment issues encountered during testing prevented full completion of the planned pressure drop test matrix using the inlet peaked assembly. As a consequence, additional data were obtained using a GNF2 test assembly with a cosine axial power shape. This data is presented in Table 2-4.

Some of the pressure drop instrumentation for various segments within the assembly were off-scale. No local  $\Delta P$  data for an upper segment are available and the corresponding far right columns of the table are blank.

Comparing the inlet peaked and cosine data tables, the integrated channel powers are either identical or very close (at  $\sim 2/3$  height or 116 – 118 inches), so the exit qualities and exit void fractions are nearly the same between the two power shapes for the same flow rates, pressure and subcooling. The calculated uncertainties ( $\delta\alpha$ ) are nearly identical to the inlet peaked data, so the conclusions derived from the inlet peaked data (Section 2.3.3.1) are unchanged.

### 2.3.4 Low Flow Test Summary

The residuals ( $\delta\alpha$ ) from all four tables of low flow data (Tables 2-1 through 2-4) are presented in Figure 2-2 and Figure 2-3. The figures do not indicate any obvious biases or trends. Even though the two GE12 high power test cases noted above could be considered to be outliers, they still lie within the expected range of results. [[

]]

## 2.4 An Alternate Approach Using High Flow Rate Tests

The analysis in the prior sections used low flow test data to examine the Findlay-Dix correlation's accuracy for a range of steam qualities (roughly 10 to 65%). However, the void correlation is typically applied to a wider range of thermal-hydraulic conditions, in particular, higher flow rates are more typical of BWR operation. It is possible to examine additional data at higher flows, but this requires a re-examination of the base assumptions used to quantify the void uncertainty.

### 2.4.1 Assumptions and Approach

In the evaluation presented in the prior section, all calculational error is assigned to the void fraction prediction through the elevation pressure drop. While  $\Delta P$  is calculated in terms of constituents, only a single, integral measured value exists for any test. The elevation head term is dominant under the low flow test conditions, so that this term is not confounded with frictional losses. In contrast, at higher flow rates, the frictional contributions to  $\Delta P$  are significant and cannot be taken as zero

$$\delta P_{Fric} \neq 0, \quad \delta P_{Loc} \neq 0, \quad \delta P_{Acc} \neq 0 \quad (2.22)$$

Under these conditions, Equation (2.7) is no longer valid, in that the error residual is no longer driven by elevation pressure drop and void fraction.

$$\delta P_{Total} \neq \delta P_{Elev} \quad (2.23)$$

The various calculated losses are added (superimposed), which raises a concern that any tendency to over or underpredict elevation losses may not accumulate in the  $\delta P_{Total}$  value due to compensating errors (bias) from the frictional terms.

The concern for compensating errors warrants further discussion. Theoretically, the biases from frictional and elevation errors could offset, resulting in unreliable estimates of the biases attributable to void term. However, the contributions to variation (uncertainties), as opposed to bias, are cumulative and do not offset.

$$\sigma_{\Delta P_{calc}}^2 = \underbrace{\left(\frac{\partial \Delta P}{\partial \alpha}\right)^2 \sigma_{\alpha}^2}_{\text{elevation head (void)}} + \underbrace{\sum_i \left(\frac{\partial \Delta P}{\partial x_i}\right)^2 \sigma_{x_i}^2}_{\text{wall friction, acceleration, and local losses}} \quad (2.24)$$

Again, it is possible that individual observations of  $\delta P_{Total}$  may contain compensating errors, which could lead to unreliable estimates of  $\delta P_{Elev}$  and  $\overline{\delta P_{Elev}}$ , which are in turn used to derive  $\delta \alpha$ . However, for collections of observations, the calculational uncertainty will have an additional component that adds to the total variation. Therefore, high flow rate data can be useful for the purpose of evaluating uncertainty, noting that assigning the total calculational uncertainty to the elevation component will over-estimate this value.

Additional detail regarding the high flow rate error residuals is provided in Appendix F, including a discussion of local versus integral errors.

#### 2.4.2 Additional Test Results

The GE14 pressure drop data presented in Figure F-3, as well as other datasets are summarized in the tables below. Table 2-5 contains a summary of the test conditions. Table 2-6 gives the corresponding data. The formulas from Sections 2.1 and 2.2 have been applied to determine the pressure drop and void fraction biases and uncertainties. The GE12 and GE14 results from the ATLAS facility have a slightly higher measurement uncertainty; the correction from Appendix D ( $\sigma_{meas}$ ) has been applied to determine the  $\sigma_{\alpha}$ . The GNF2 data is uncorrected for measurement uncertainty.

The test assemblies were configured into a variety of peaking patterns for the experiments and appropriately represent modern fuel designs in reactor applications. [[

]]

**Table 2-5 10x10 Pressure Drop Test Conditions**

Test Series		Thermal-Hydraulic Test Conditions				
Assembly	Axial Power Shape	Power (MWt)	Mass Flux Mlbm/hr-ft <sup>2</sup> (kg/m <sup>2</sup> -s)	System Pressure psia (MPa)	Inlet Temp. °F (C)	Exit Steam Quality <sup>16</sup>
[[						
						]]

**Table 2-6 10x10 Pressure Drop Test Data Summary**

Test Series	No. Points	Ave. Err. ( $\delta P$ – psid)	Std. Dev. ( $\sigma_{\delta P}$ – psid)	Ave. Err. ( $\delta \alpha$ )	Std. Dev. ( $\sigma_{\alpha}$ )
[[					
17					]]

<sup>16</sup> Low power-to-flow ratio cases are included (but no 0.0 MWt cases). [[

]]

<sup>17</sup> Combined as shown in Appendix E.

The GE14 (Table 2-2) and GNF2 cosine (Table 2-4) tests are not included in the high flow rate assessment. These tests used a slightly different inlet configuration, which introduces a slight  $\Delta P$  bias at higher power and flow rates.

### 2.4.3 Alternate Approach Summary

The 10x10 void fraction uncertainty derived from full assembly  $\Delta P$  data matches the original Findlay-Dix database reasonably well. Relative to the low flow data, the approach incorporates additional sources of error over the broader range of thermal-hydraulic conditions (such as the frictional or  $\delta P \propto G^2$  tendency depicted by Figure F-5). Some of the additional error is also due to measurement uncertainty. Several key measurement uncertainties are proportional to test parameters, such as flow rate and power level. For the ATLAS based data, a correction for  $\sigma_{meas}$  is applied.

Using the  $\Delta P$  error residuals over the broader range of thermal hydraulic conditions to estimate void fraction residual errors, the combined uncertainty of the 10x10 data is virtually identical to the uncertainty for the 8x8 validation datasets (3.9%). The mean errors (bias values) are also similar and the data falls within the tolerance interval representing the Findlay-Dix database.

## 2.5 Comparison Summary

Pressure drop information has been gathered from full-scale thermal hydraulic experiments for 10x10 fuel designs. The physical and calculational relationships between void fraction and pressure drop in a BWR channel makes it possible to perform quantitative assessments of void fraction bias and uncertainty. Two approaches to evaluating error residuals (predicted versus measured) are presented.

- Low flow rate comparisons – In these cases, comparisons were limited to flow rates where friction, acceleration, and local (form) losses are minimized. Under these conditions, the calculated and measured  $\Delta P$  is a strong function of void fraction. This allows  $\Delta P$  error residuals to be converted to void fraction error residuals, which can be compared to the original Findlay-Dix database.
- Alternate approach (extended flow range) comparisons – In these cases, the low flow rate approach is essentially repeated for a broader set of power/flow conditions. Under these conditions, the accuracy of  $\Delta P$  predictions depends on more than just void fraction. The  $\delta P$  error residuals contain contributions from the predictions of the other pressure drop constituent terms  $\Delta P_{local}$ ,  $\Delta P_{fric}$ , and  $\Delta P_{acc}$ , in addition to the contribution from  $\Delta P_{elev}$ . Close examination of error residuals from these tests (Appendix F) shows the variation or uncertainty is over-estimated using this approach.

Both the low flow rate comparisons and the extended thermal-hydraulic range evaluations in Section 2.4 compare well with the 8x8 validation dataset uncertainty. The uncertainty in

NEDO-33173 Supplement 1, Revision 0  
Non-Proprietary Information

predicted void fraction for 10x10 fuel designs does not appear to be different from the ASEA multi-rod data used to validate the Findlay-Dix correlation.

### **3.0 BENCHMARK CALCULATIONS**

#### **3.1 Alternative Approaches to Void Fraction Predictions**

The drift flux model discussed in Section 1.2 is widely applied to engineering analyses of two-phase systems. The model is typically used in conjunction with one-dimensional separated flow (mixture) conservation equations. In a sense, the drift flux model can be thought of as a two-phase equation of state necessary to complete the equation set [25]. Another popular approach used to model two-phase flows utilizes a set of two-fluid conservation laws with interface exchange [26] models. This approach is similar to the separated flow treatment (time and spatial averaging). However, instead of relying on a drift flux model, this approach employs closure laws for the interface. Key features of computer programs that use this approach include the use of a flow regime map, interfacial and wall shear models, and interfacial and wall heat transfer models.

This section summarizes comparisons between the Findlay-Dix correlation and alternative methods based on interface exchange models. Steady state comparisons between TRACG (one dimensional), COBRAG (multi-dimensional), the Findlay-Dix correlation (1-D empirical), and experimental data are presented.

##### **3.1.1 The COBRAG Model**

COBRAG [21] is a steady state subchannel analysis code, which can be used to predict the critical power and dryout location, local and bundle planar average void fraction, and pressure drop of BWR fuel bundles. It is capable of simulating a broad range of bundle geometries. Bundles with large water rods, part length rods, and full-length rods can be modeled with their own specific size, axial power profile, and local peaking. Bundle inlet and outlet conditions, including inlet flow distributions, can be simulated as boundary conditions and specified by input.

The subchannel two-phase flow is described by a two-fluid, multi-field model. The two fluids represented within COBRAG are the vapor and liquid phases, which are used to treat three distinct fields. The three fields are continuous vapor or bubbles, continuous liquid or droplets, and liquid films. The model treats the conservation equations of mass, momentum and energy for these fields in the two-phase flow. Interactions between the fields are modeled through constitutive correlations for interfacial shear and heat transfer, entrainment and deposition. Inter-subchannel transport phenomena like mixing and void drift are also modeled. Energy transfer from the channel wall is modeled as a boundary condition. Physical models include a full or part length rod model with its own specific axial power profile and peaking factor, and a semi-empirical spacer model.

COBRAG has been qualified against experimental data for void fraction, pressure drop, and critical power (dryout) over a wide range of thermal hydraulic conditions. The comparisons

include simple geometry experiments (e.g., tubes and annuli), as well as various rod arrays (e.g., 4x4, 6x6, 8x8, 9x9, and 10x10). These experiments include a variety of power profiles and local peaking patterns. A subset of these cases are presented below.

### **3.1.2 The TRACG Model**

TRACG [27] is GE's version of the TRAC code. Like its predecessors, TRAC-PF1/MOD1 and TRAC-BF1/MOD1, the GE version uses a two-phase, two-fluid model for fluid flow in both the one-dimensional (1-D) and three-dimensional (3-D) components. Kocamustafaogullari [28] and Ishii [29] have provided detailed derivations of the equations similar to those used in TRAC, and a more concise derivation related to the TRACG equations is available in a report by Addressio [30]. Closure relations include expressions for interfacial-drag, interfacial heat transfer, the phase-change rate (evaporation and condensation), wall shear and wall heat flow.

TRACG uses a specialized CHAN component to model BWR fuel bundles. The CHAN component is essentially a 1-D channel with a set of heat transfer models suitable for representing the fuel rods. TRACG has been extensively qualified through comparisons to experimental data, including void fraction data. TRACG based results are presented together with COBRAG results (planar average void fraction) for the FRIGG tests (Section 3.2.1).

## **3.2 Benchmark Results**

### **3.2.1 OF-64 Data**

The OF-64 tests (ASEA 713 test series from Table 1-1 in Section 1.3) were one of the development datasets for the Findlay-Dix correlation. Planar average void fraction data from these tests have also been used to validate TRACG and COBRAG predictions. TRACG and COBRAG comparisons are shown in Figure 3-1 through Figure 3-5. A summary of these comparisons is provided in Table 3-1. The Findlay-Dix statistics were taken directly from Appendix F of NEDE-21565. Appendix F gives the detailed statistics for the broader OF-64 test series.

The tabular and graphical data represent a sample from the OF-64 test series. The void fraction results agree well between the different methods.



**Table 3-1      Average Error ( $\Delta\alpha = \alpha_m - \alpha_c$ ) and Standard Deviation Comparisons for Planar  
Average Void Fractions**

Run No.	No. of Points	Findlay-Dix		TRACG		COBRAG	
		Ave. Error	Std. Dev.	Ave. Error	Std. Dev.	Ave. Error	Std. Dev.
[[							
							]]

---

<sup>18</sup> Combined as shown in Appendix E.

[[

]]

**Figure 3-1    OF-64 Test 001**

[[

]]

**Figure 3-2    OF-64 Test 013**

[[

]]

**Figure 3-3    OF-64 Test 014**

[[

]]

**Figure 3-4    OF-64 Test 019**

[[

]]

**Figure 3-5 OF-64 Test 040**

### **3.2.2 NUPEC 8x8 Data**

The Nuclear Power Engineering Corporation (NUPEC) of Japan has made two-phase flow benchmarking data available. Over a period from 1987 to 1995, NUPEC conducted an experimental program using full-scale tests to examine the performance of both PWR and BWR fuels. The BWR full-size Fine-mesh Bundle Test (BFBT) benchmark [31] consists of highly resolved void fraction and critical power data. The data was collected from a system using two measurement techniques, X-ray Computer Tomography (CT) and X-ray densitometry. The CT system was applied to the steady state tests. This system was capable of resolving “pixel” level elements (0.3 mm x 0.3 mm). In addition to the detailed steady state void distributions, the CT system was used to reconstruct subchannel (400 pixel elements) and cross sectional averaged ( $10^5$  pixel elements) void distributions.

The BFBT data was taken from a full-scale, electrically heated replicas of BWR fuel bundles. Test assembly #4 represents a GE9 fuel bundle, which is a 8x8 design with a large central water rod. The (single) water rod takes up the four central fuel rod positions within the 8x8 lattice. The radial peaking pattern that was tested is shown in Table 3-2. Note that the bundle radial peaking pattern is edge peaked and nearly symmetric. Also, this particular test assembly used uniformly heated rods, i.e., the axial power profile was uniform.

**Table 3-2      BFBT Bundle Local Peaking Factor Array for Assembly #4**

(i, j)	1	2	3	4	5	6	7	8
1	1.15	1.30	1.15	1.30	1.30	1.15	1.30	1.15
2	1.30	0.45	0.89	0.89	0.89	0.45	1.15	1.30
3	1.15	0.89	0.89	0.89	0.89	0.89	0.45	1.15
4	1.30	0.89	0.89			0.89	0.89	1.15
5	1.30	0.89	0.89			0.89	0.89	1.15
6	1.15	0.45	0.89	0.89	0.89	0.89	0.45	1.15
7	1.30	1.15	0.45	0.89	0.89	0.45	1.15	1.30
8	1.15	1.30	1.15	1.15	1.15	1.15	1.30	1.15

### 3.2.2.1 Planar Average Void Fraction Comparisons

A set of steady state BFBT tests were chosen for comparison to COBRAG and the Findlay-Dix correlation. The test conditions are given in Table 3-3, which essentially shows four mass flux values and constant pressure and inlet subcooling. The assembly powers were varied, resulting in different exit qualities. Figure 3-6 through Figure 3-9 shows void fraction versus quality for these tests. A summary of predicted versus measured void fraction values is presented as Figure 3-10. The statistics for these comparisons (e.g., Equation (E.9) from Appendix E) are  $0.015 \pm 0.020$  for COBRAG and  $0.004 \pm 0.024$  for the Findlay-Dix correlation. COBRAG and the Findlay-Dix correlation agree well.

NEDO-33173 Supplement 1, Revision 0  
Non-Proprietary Information

**Table 3-3      BFBT Test Series for Assembly 4 – Test Conditions**

Test ID	Pressure (MPa)	Subcooling (kJ/kg)	Mass Flux (kg/m <sup>2</sup> -s)	Assembly Power (MW)	Exit Quality
4101-39	7.15	51.5	588.5	0.45	0.02
4101-40	7.14	52.0	588.0	0.70	0.05
4101-41	7.13	50.5	588.0	0.96	0.08
4101-42	7.14	52.0	588.0	1.29	0.12
4101-43	7.14	50.5	588.8	1.79	0.18
4101-44	7.14	50.6	589.7	2.36	0.25
4101-45	7.17	52.2	878.9	0.69	0.02
4101-46	7.16	51.2	878.6	1.06	0.03
4101-47	7.13	50.6	878.9	1.43	0.08
4101-48	7.17	51.2	878.0	1.93	0.12
4101-49	7.17	51.2	878.9	2.67	0.18
4101-50	7.18	50.3	878.0	3.55	0.25
4101-54	7.19	52.7	1603.6	1.23	0.02
4101-55	7.20	52.9	1602.4	1.92	0.05
4101-56	7.18	51.8	1603.3	2.59	0.08
4101-58	7.15	50.6	1602.1	3.52	0.12
4101-59	7.19	52.1	1601.9	4.88	0.18
4101-61	7.18	52.5	1604.2	6.48	0.25
4101-64	7.16	53.6	2041.0	1.57	0.02
4101-65	7.16	52.8	2041.0	2.44	0.05
4101-66	7.20	52.9	2045.7	3.32	0.08
4101-67	7.25	54.6	2042.5	4.48	0.12
4101-68	7.28	56.0	2041.9	6.22	0.18



[[

]]

**Figure 3-6     Test Series 4101-39 Through 44 ( $G = 588 \text{ kg/m}^2\text{-s}$ )**

[[

]]

**Figure 3-7     Test Series 4101-45 Through 50 ( $G = 878 \text{ kg/m}^2\text{-s}$ )**

[[

]]

**Figure 3-8     Test Series 4101-54 Through 61 ( $G = 1,600 \text{ kg/m}^2\text{-s}$ )**

[[

]]

**Figure 3-9      Test Series 4101-64 Through 68 ( $G = 2,040 \text{ kg/m}^2\text{-s}$ )**

[[

]]

**Figure 3-10 Test Summary – Predicted Versus Measured Planar Average Void Fraction**

### **3.2.2.2 Subchannel (Regional) Void Fraction Comparisons**

As discussed in Section 3.1.1, COBRAG solves conservation equations for each field of interest, i.e., liquid films, vapor, and droplets, which exist in the annular flow regime under high void fraction conditions. The model considers interactions between the fields, such as evaporation, entrainment, deposition, and void drift. These models enable COBRAG to treat the subchannel spatial scale, and with some degree of confidence, resolve the in-channel void distribution. This approach is more physics-based than an empirical void-quality correlation, and is extensible to different array sizes.

Figure 3-11 through Figure 3-14 shows COBRAG predictions versus NUPEC data for regional void distributions. For these cases, the void fraction for each “ring” is shown, where the value has been averaged over area

$$\langle \alpha \rangle = \frac{1}{A} \iint_A \alpha dA \approx \frac{\sum_i \alpha_i A_i}{\sum_i A_i} \quad (3.1)$$

The  $\alpha_i$  and  $A_i$  represent the subchannel void fractions and corresponding areas. The regions or “rings” essentially correspond to the areas or spaces between the rows of rods in the array; they are numbered 1 through 4, starting closest to the water rod and increasing outward. Rings 1 and 4 contain the unheated surfaces, namely the water rod and channel box, respectively. Rings 2 and 3 are the interior most rings with no unheated surfaces. Rings 2 and 3 make up 60% of the total cross sectional area, where ring 1 only represents about 9% of the total.

Considering Figure 3-11 as an example, the data shows differences between the various regions in the bundle. For example, at roughly 40% average void fraction, the regional measured void fractions vary from 33% up to 46%. At higher average void levels, the data indicates less of a difference between rings. The COBRAG predictions properly reflect this trend.

[[

]]

**Figure 3-11 Predicted Versus Measured Radial Void Profiles ( $G = 588 \text{ kg/m}^2\text{-s}$ )**

[[

]]

**Figure 3-12 Predicted Versus Measured Radial Void Profiles ( $G = 878 \text{ kg/m}^2\text{-s}$ )**

[[

]]

**Figure 3-13 Predicted Versus Measured Radial Void Profiles ( $G = 1,600 \text{ kg/m}^2\text{-s}$ )**



[[

]]

**Figure 3-14 Predicted Versus Measured Radial Void Profiles ( $G = 2,040 \text{ kg/m}^2\text{-s}$ )**

The comparisons show a slight trend in the outer ring (#4). Figure 3-12 shows a discrepancy at low quality (run 45). At higher flow rates, the degree of discrepancy increases and also appears in the higher quality runs (e.g., runs 54 and 55 in Figure 3-13, then runs 64, 65, and 66 in Figure 3-14). The ring 4 disagreement appears to increase with mass flux. Given the inconsistency in the comparisons, it is worthwhile to closely examine the NUPEC data before making judgements regarding the performance of the COBRAG models. As shown in Table 3-2, the peaking in the simulated bundle is very nearly symmetric. Intuitively, this would imply that the measured void distributions should also be symmetric. However, some of the measured subchannel void distributions show a strong degree of asymmetry. For example, consider run 4101-55 as shown in Figure 3-13. The measured subchannel void fraction in the outer (1,1) corner, which would be

in ring 4, is 0.33. However, the measured subchannel void fraction in the opposite corner, outside of rod position (8,8) is 0.42, which is significantly different<sup>19</sup> and not self-consistent.

The degree of asymmetry can be characterized by calculating the regional void fraction differences in the data. This is shown in Figure 3-16, which shows the maximum difference between planar average void fraction values based on “quadrants,” or regions as shown in Figure 3-15. The quadrants correspond to the water rod as the origin, so that the upper right quadrant is I, the upper left is II, etc., analogous to a two-dimensional cartesian grid. The asymmetry points are simply  $\Delta\alpha = \max|\alpha_i - \alpha_j|$ , where the (i, j) subscripts represent any of the  $\alpha_I$ ,  $\alpha_{II}$ ,  $\alpha_{III}$ , and  $\alpha_{IV}$  (area averaged) measurement values. For symmetric, steady state conditions, the  $\Delta\alpha$  should be small. However, this is not the case. The data shows a trend in  $\Delta\alpha$ , indicating an increase in the degree of asymmetry with mass flux. Local (individual subchannel or smaller region) asymmetries can be much higher than shown in the figure, as discussed above.

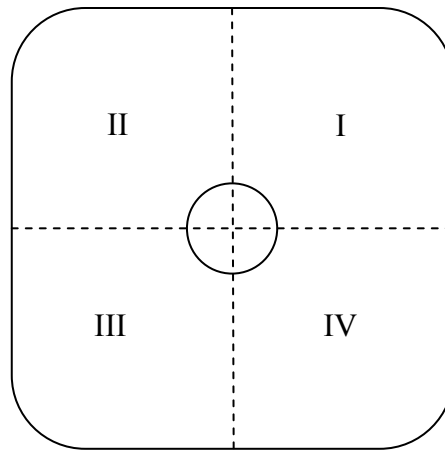


**Figure 3-15 Quadrants for the Regional Void Fraction Asymmetry Evaluation**

The source of the asymmetry in the measurement is unknown, so any suggestions regarding an assignable cause are speculative. Noting this, however, the observed variation could be explained by unintentional changes in test parameters, such as variations in subchannel flow areas (e.g., due to the assembly shifting relative to channel gaps or tolerance). Glück [32] makes similar observations and adds a concern for the transient effects or inherent fluctuations in the flow relative to the measurement times. The COBRAG predictions are based on symmetric subchannel areas; the combination of symmetric channel geometry (areas) and peaking will always produce a symmetric calculated void distribution. Regardless of the cause of the variation in the data, its existence must be considered in interpreting the results and examining comparisons against computer models.

---

<sup>19</sup> Reference [31] gives the subchannel uncertainty for the CT scanning system as 3%. The uncertainty in the planar average void fraction is 2%.

Based on Figure 3-16, the lower mass flux comparisons appear to be less susceptible to asymmetry. The results are self-consistent and provide for better overall comparisons with COBRAG. For these more reliable datapoints, the COBRAG results agree well. For example, Figure 3-11 (0.43 Mlbm/hr-ft<sup>2</sup>) and Figure 3-12 (0.65 Mlbm/hr-ft<sup>2</sup>) demonstrate COBRAG's capability to properly capture the radial void profile across the lattice; note that these conditions represent the highest power-to-flow ratios from the set that is presented. Also, as demonstrated by the other figures, the interior regions (e.g., rings 2 and 3) are less susceptible to this issue and agree reasonably well, even at the upper mass fluxes. Since these regions tend to represent the majority of the cross sectional area within the bundle, the calculated overall averages also agree well for the comparison set, as demonstrated by the Section 3.2.2.1 results.

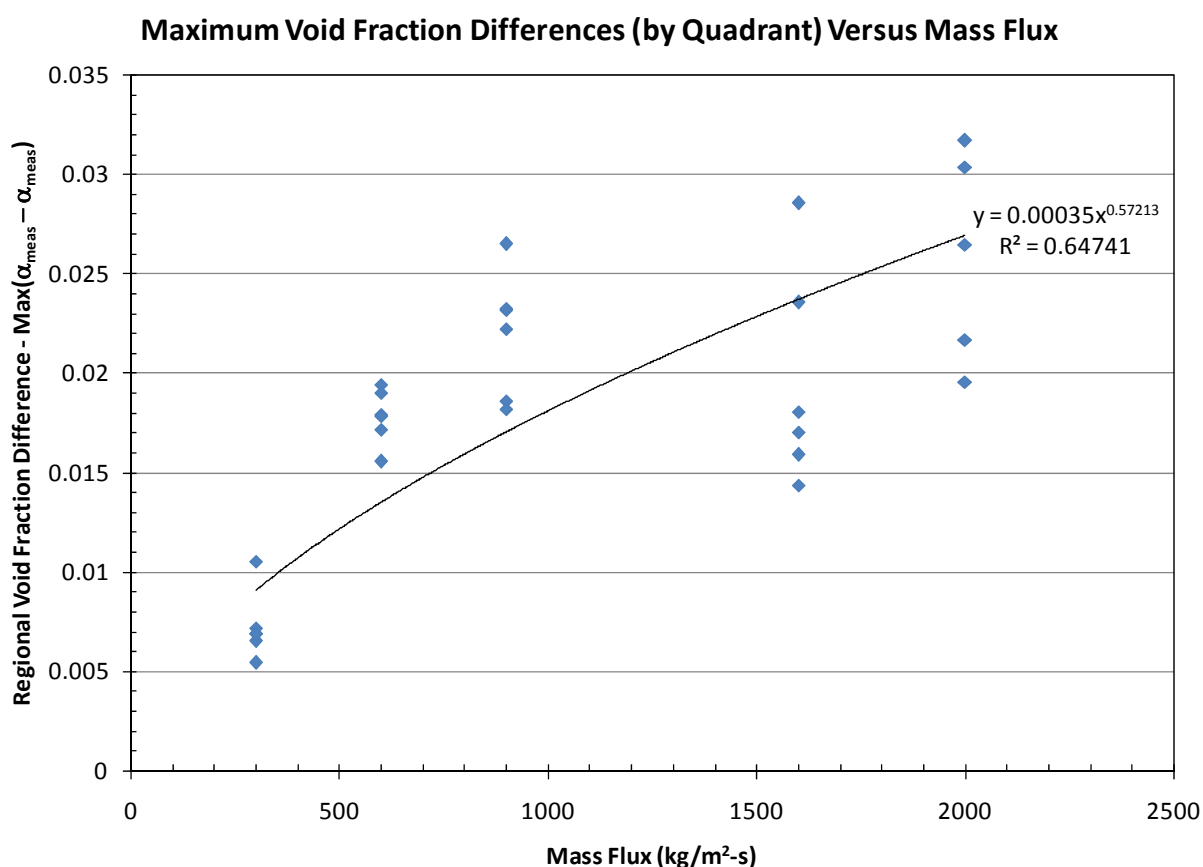


**Figure 3-16 NUPEC Regional Void Fraction Asymmetry Versus Mass Flux**

### 3.2.3 GNF2 10x10 Benchmark Comparisons

#### 3.2.3.1 Planar Average Void Fraction Comparisons

A set of GNF2 benchmark cases is presented in this section. These cases are part of the GNF2 steady state critical power database and have been simulated with COBRAG (the inlet and outlet

peaked cases are discussed in Reference [34]). The test conditions are shown in Table 3-4. For each of these cases, the COBRAG model was applied to predict boiling transition (i.e., film dryout).

**Table 3-4      GNF2 Benchmark Cases – Test Conditions**

<b>Case ID</b>	<b>Axial Power Shape</b>	<b>Mass Flux Mlbm/hr-ft<sup>2</sup> (kg/m<sup>2</sup>-s)</b>	<b>Pressure psia (MPa)</b>	<b>Subcooling BTU/lbm (kJ/kg)</b>	<b>Assembly Power MWt</b>
[[					
					]]

Figure 3-17 shows the predicted void fraction trend for the cases given in Table 3-4. Results based on both COBRAG and the Findlay-Dix correlation are shown. The results were obtained by taking the predicted nodal average void fraction values and plotting them versus the node (exit) steam flow qualities. The predicted trend is consistent with Figure 1-1, which is presented in Section 1.4.3.1.

Figure 3-18 shows the Findlay-Dix void fraction values versus the corresponding COBRAG planar average void fractions. The values are based on point-by-point (axial) comparisons of the Table 3-4 cases. The three cases form a set of 81 comparison points that span a wide range of steam qualities. The void fraction mean error (error residuals for the COBRAG versus Findlay-Dix comparison points) is -0.005, with a standard deviation of 0.007, which indicates excellent agreement.

[[

]]

**Figure 3-17 Predicted Void Fraction Trend for GNF2**

[[

]]

**Figure 3-18 GNF2 Void Fraction Predictions – Findlay-Dix vs. COBRAG**

### **3.3 Benchmark Summary**

Several sets of benchmark calculations are presented. Section 3.2.1 shows comparisons to the OF-64 (ASEA-713 test series) 8x8 data using the Findlay-Dix (drift flux) correlation, as well as two methods based on interface exchange models (TRACG and COBRAG). Section 3.2.2 shows comparisons to several NUPEC 8x8 experiments, which includes both planar average and more detailed (subchannel) void fraction data. Both Findlay-Dix and COBRAG predict the average void fraction well. Also, comparing COBRAG-based predictions to the NUPEC data demonstrates COBRAG's capability to reasonably resolve the in-channel void distribution based on multi-dimensional conservation equations, interface closure relations, and detailed geometry and peaking information. Finally, Section 3.2.3 presents Findlay-Dix and COBRAG comparisons for 10x10 geometry. These GNF2 benchmarks represent an extension of the mechanistic COBRAG modeling approach to modern 10x10 fuel designs. The comparisons to COBRAG indicate that the Findlay-Dix correlation performs well, which is consistent with the results of the pressure drop based uncertainty evaluation presented in Section 2.0.

## 4.0 CONCLUSIONS

### 4.1 Summary

In Section 1.0, an overview of the Findlay-Dix correlation, its technical basis and application within GE safety analysis methodologies is presented. Each methodology utilizing the Findlay-Dix correlation is summarized with a brief discussion of its qualification basis. In general, safety margins established with GE analysis methods include provisions for relevant uncertainties. However, in the PANAC-ODYN suite of methods, void fraction uncertainty is not treated explicitly. Void uncertainty is swept into the uncertainties in other parameters, such as power. In order to preserve the existing qualification bases, which provide the foundations for core and fuel safety margins, it is important that the Findlay-Dix prediction uncertainty remains consistent with its established database. The approach taken here is to demonstrate consistency when the correlation is applied to 10x10 fuel.

Section 2.0 outlines an approach for relating void fraction residual error to pressure drop residual error. This approach allows quantitative evaluations of void fraction bias and uncertainty based on full-scale, steady state experimental data. Transient comparisons are not presented; as noted in Section 1.4, the ODYN-TASC methodology includes transient qualification for 10x10 fuel designs. Two sets of evaluations are presented. The comparisons to low flow experiments give 10x10 bias and uncertainty values comparable to the original 8x8 validation datasets. Comparisons over a broader range of channel flow rates and power levels also yields uncertainty values that compare well with the historical validation datasets. The experiments cover a range of void fractions that would be expected in BWR operation, which includes channel conditions expected in expanded operating domains (Appendix B).

Additional benchmark cases are presented in 3.0. Both the Findlay-Dix correlation (empirical) and methods relying on interface exchange models agree with 8x8 experimental data. COBRAG is compared against additional data to demonstrate the ability of the more detailed model to predict local (regional) void fractions. Finally, COBRAG and Findlay-Dix are compared to 10x10 cases. The 10x10 calculations represent simulations of critical power tests where COBRAG has been applied to predict (match) critical power, which also implies high void fraction conditions. These cases show very close agreement.

The uncertainty evaluation based on 10x10 test data and the numerical benchmarks are confirmatory. The results indicate that 10x10 void fraction predictions based on Findlay-Dix have retained a consistent level of accuracy relative to the correlation's original basis. It is important to note that this result is not unexpected, in that it is consistent with other information. The correlation itself is the result of a development effort that was driven by a need to improve BWR prediction accuracy. While the prior design correlation (Dix) performs quite well when compared to a wide range of experiments [1], GE's experience has shown that void fraction inaccuracy can manifest itself in mispredictions of observable core parameters and

instrumentation (e.g., TIPS). However, indirect evidence from nuclear comparisons also indicate that the Findlay-Dix correlation has retained a consistent level of accuracy in modern BWR applications.



## 5.0 REFERENCES

- [1] Paul Coddington and Rafael Macian, “A Study of the Performance of Void Fraction Correlations Used in the Context of Drift-Flux Two-Phase Flow Models,” Nuclear Engineering and Design, Vol. 215, No. 3, pp. 199-216 (June 2002).
- [2] MFN-07-189, Stacey L. Rosenberg (NRC) to Robert E. Brown (GEH), “Draft Safety Evaluation for General Electric (GE) Nuclear Energy (GENE) Licensing Topical Report (LTR) NEDC-33173P, ‘Applicability of GE Methods to Expanded Operating Domains,’ TAC No. MD0277,” March 14, 2007.
- [3] Mamoru Ishii and Takashi Hibiki, “Thermo-Fluid Dynamics of Two-Phase Flow,” Springer Science, 2006.
- [4] R.T. Lahey, Jr. and F.J. Moody, “The Thermal-Hydraulics of a Boiling Water Nuclear Reactor,” ANS Monograph, 1977.
- [5] Takashi Hibiki and Mamoru Ishii, “One-Dimensional Drift-Flux Model and Constitutive Equations for Relative Motion Between the Phases in Various Two-Phase Flow Regimes,” International Journal of Multiphase Heat and Mass Transfer, 46 (2003) 4935–4948.
- [6] Spore, J.W. and Shiralkar, B.S., “A Generalized Computational Model for Transient Two-Phase Thermal-Hydraulics in a Single Channel,” NR-13, pp. 71-76, Sixth International Heat Transfer Conference, Toronto, 1978.
- [7] Ishii, M., “One-Dimensional Drift-Flux Model and Constitutive Equations for Relative Motion Between the Phases in Various Two-Phase Flow Regimes,” Argonne National Laboratory, ANL-77-47, October 1977.
- [8] John G. Collier and John R. Thome, “Convective Boiling and Condensation,” Oxford Science Publications, 3rd Ed., 1996.
- [9] NEDE-21565, “BWR Void Fraction Correlation and Data,” January 1977.
- [10] MFN-003-86, J.S. Charnley (GE) to H.N. Berkow (NRC), “Revised Supplementary Information Regarding Amendment 11 to GE Licensing Topical Report NEDE-24011-P-A,” January 16, 1986.
- [11] X.M. Chen and J.G.M. Andersen, “Dynamics in BWR Fuel Bundles During Transients,” Ninth International Topical Meeting on Nuclear Thermal Hydraulics (Proc. NURETH-9), San Francisco, California, October 1999.
- [12] MFN 06-211, Bob E. Brown (GE) to US Nuclear Regulatory Commission Document Control Desk, “Compilation of Responses to Methods RAIs – Interim Methods LTR,” July 18, 2006.

NEDO-33173 Supplement 1, Revision 0  
Non-Proprietary Information

- [13] NEDE-24011-P-A-16-US, “General Electric Standard Application for Reactor Fuel (GESTAR II),” October 2007.
- [14] NEDO-31908, “Licensing Criteria for Fuel Designs, Amendment 22 to NEDE-24011-P-A and Corresponding NRC Staff Safety Evaluation,” January 1991.
- [15] NEDE-13181, “An Experimental and Analytical Study of the Synthesis of Grid Spacer Loss Coefficients,” March 1971.
- [16] NEDC-32601P-A, “Methodology and Uncertainties for Safety Limit MCPR Evaluations,” August 1999, Attachment A, “BWR Fuel Void Fraction.”
- [17] Tsuyoshi Ama, Hideaki Hyoudou, and Toshikazu Takeda, “Effect of Radial Void Distribution Within Fuel Assembly on Assembly Neutronic Characteristics,” Journal of Nuclear Science and Technology, Vol. 39, No. 1, pp. 90-100 (January 2002).
- [18] MFN 098-96, Ralph J. Reda (GE) to R.C. Jones, Jr. (NRC), “Implementation of Improved GE Steady-State Nuclear Methods,” July 2, 1996.
- [19] Hiroshi Shirai, Hisashi Ninokata, Akitoshi Hotta, Takashi Hara, “Analytical Study on Detailed Void Distributions Inside a BWR Fuel Bundle Under Turbine Trip Event Considering Time-Dependent Pin Power Distributions,” Journal of Nuclear Science and Technology, Vol. 39, No. 11, pp. 1152-1161, November 2002.
- [20] X.M. Chen and J.G.M. Andersen, “Prediction of Cross Sectional Void Distribution in a BWR Fuel Bundle Configuration,” Eighth International Topical Meeting on Nuclear Thermal Hydraulics (Proc. NURETH-8), Kyoto, Japan, September 1997.
- [21] FLN-2007-023, “Transmittal of GNF Report ‘COBRAG Subchannel Code – Model Description Report,’ NEDE-32199P, Revision 1, July 2007, Supporting the GE ESBWR Design Control Document,” July 5, 2007.
- [22] MFN 09-552, “NEDE-33173P, Revision 2 and Supplement 2, Parts 1-3 – Analysis of Gamma Scan Data and Removal of Safety Limit Critical Power Ratio (SLMCPR) Margin,” August 14, 2009.
- [23] F. Jatuff, F. Giust, J. Krouthén, S. Helmersson, R. Chawla, “Effects of Void Uncertainties, on the Void Reactivity Coefficient and Pin Power Distributions for a 10x10 BWR Assembly,” Annals of Nuclear Energy 33 (2006), pp. 119-125.
- [24] Tadashi Ikehara, Yoshiro Kudo, Masashi Tamitani, Munenari Yamamoto, “Effect of Subchannel Void Fraction Distribution on Lattice Physics Parameters for Boiling Water Reactor Fuel Bundles,” Journal of Nuclear Science and Technology, Vol. 45, No. 12, pp. 1237-1251, July 2008.
- [25] NEDO-13388, “Two-Phase Flow in Boiling Water Nuclear Reactors,” July 1974.
- [26] Salomon Levy, “Two-Phase Flow in Complex Systems,” John Wiley & Sons, 1999.

NEDO-33173 Supplement 1, Revision 0  
Non-Proprietary Information

- [27] NEDE-32176P, “TRACG Model Description,” Rev. 4, January 2008.
- [28] G. Kocamustafaogullari, “Thermo-Fluid Dynamics of Separated Two-Phase Flow,” Ph. D. thesis, Georgia Institute of Technology, December 1971.
- [29] M. Ishii, “Thermo-Fluid Dynamic Theory of Two-Phase Flow,” Collection de la Direction des Études et Recherches D’Électricité de France, Eyrolles, Paris, 1981.
- [30] F. L. Addessio, “A Review of the Development of Two-Fluid Models,” NUREG/CR-2146, August 1981.
- [31] NEA/NSC/DOC(2005)5, “NUPEC BWR Full-size Fine-mesh Bundle Test (BFBT) Benchmark, Volume I: Specifications,” Copyright OECD 2006, ISBN 92-64-01088-2.
- [32] M. Glück, “Validation of the sub-channel code F-COBRA-TF, Part II. Recalculation of void measurements,” Nuclear Engineering and Design, 238 (2008) 2317-2327, February 2008.
- [33] Crow, Davis, and Maxfield, “Statistics Manual,” Dover Publications, Inc., New York, 1960.
- [34] NEDC-33320P, “COBRAG Subchannel Analysis of the GNF2 10x10 Bundle,” Rev. 0, July 2007.

## APPENDIX A      NOMENCLATURE AND ACRONYMS

Item	Description
A	Area
ADS	Automatic Depressurization System
AOO	Anticipated Operational Occurance
D	Diameter
e	internal energy
F	Force
f	interfacial shear
g	acceleration of gravity
$\vec{g}$	gravity vector
h	specific enthalpy, $h = e + \frac{P}{\rho}$
$h_{fg}$	latent heat of evaporation, $h_{fg} = h_g - h_f$
j	volumetric flux or superficial velocity
k	Constant (e.g., loss coefficient)
LHGR	Linear Heat Generation Rate
LHS	Left Hand Side
LTR	Licensing Topical Report
$\dot{m}$	Mass flow rate
MCPR	Minimum Critical Power Ratio
P	pressure

NEDO-33173 Supplement 1, Revision 0  
Non-Proprietary Information

Item	Description
PLR	Part Length Rod
$\dot{Q}$ or $q$	heat transfer rate
RHS	Right Hand Side
RMS	Root Mean Square
S	Slip ratio
SDM	Shut Down Margin
T	temperature
TIP	Traversing In-core Probe
t	Time or “thermal”
u	Speed or velocity
V	volume
v	velocity
w	Mass flow rate
X or x	Steam quality or direction
z	axial dimension
<b>Greek Symbols</b>	
$\alpha$	gas volume fraction
$\Delta$ or $\delta$	Small or incremental change
$\Sigma$	Summation
$\rho$	microscopic density
$\sigma$	surface tension or standard deviation

NEDO-33173 Supplement 1, Revision 0  
Non-Proprietary Information

Item	Description
$\tau$	shear stress
<b>Subscripts</b>	
$f$	saturated liquid
$g$	saturated steam
$i$	Interface or index number
$j$	Index number
$\ell$ or liq	liquid phase
$r$	relative (vapor-liquid)
$s$	Steam
sat	Saturation
sub	subcooled
$v$	gas phase (mixture)
$w$	Wall

## APPENDIX B ONE-DIMENSIONAL FLOW QUALITY, EQUILIBRIUM QUALITY, AND VOID FRACTION

### B.1 Quality

Consider a simple (one-dimensional) heated channel or duct under steady state conditions. In this case, the energy storage rate is zero. The energy in-flow is equal to the energy out-flow.

$$\underbrace{\dot{m}e + \frac{d(\dot{m}e)}{dz}\delta z}_{OUT} = \underbrace{\dot{m}e + \dot{q}'(z)\delta z}_{IN} \quad (B.1)$$

Neglecting viscous dissipation, as well as the kinetic and potential energy changes, the energy per unit mass is simply the enthalpy. Integrating Equation (B.1) from the inlet to some arbitrary point  $\xi$

$$[\dot{m}h]_{z=\xi} - [\dot{m}h]_{z=0} = \int_0^{z=\xi} \dot{q}'(z)dz \quad (B.2)$$

Considering the case where vapor is generated, conservation of mass can be written

$$\dot{m}_{out} = \dot{m}_{in} = \dot{m}_{Tot} = \dot{m}_g + \dot{m}_{liq} \quad (B.3)$$

The liquid may be subcooled in a general case, but the vapor phase is treated as saturated. Both phases are considered at the same pressure. Substituting, Equation (B.2) can be written

$$\dot{m}_g h_g + \dot{m}_{liq} h_{liq} = \dot{m}_{in} h_{in} + \int_0^{z=\xi} \dot{q}'(z)dz \quad (B.4)$$

where the “in” subscript indicates the channel inlet values at  $z = 0$ . Introducing the definition of flow quality

$$X = \frac{\dot{m}_g}{\dot{m}_g + \dot{m}_{liq}} \quad (B.5)$$

Equation (B.4) can be written

$$Xh_g + (1 - X)h_{liq} = h_{in} + \frac{1}{\dot{m}_{Tot}} \int_0^{z=\xi} \dot{q}'(z)dz \quad (B.6)$$

In Equation (B.6), the liquid enthalpy and quality are functions of “z.” For subcooled boiling, another relation is necessary to partition the heat addition. Some energy is applied as sensible heat to raise the bulk fluid enthalpy, while the balance produces vapor. Regardless, the net energy addition to the fluid is strictly a function of the linear heat addition rate. Defining a bulk enthalpy for the two-phase mixture as

$$\bar{h}(z) = h_{in} + \frac{1}{\dot{m}_{Tot}} \int_0^{z=\xi} \dot{q}'(z) dz \quad (B.7)$$

Using (B.7), Equation for the flow quality can be written in terms of enthalpy (energy addition)

$$X(z) = \frac{\bar{h}(z) - h_{liq}}{h_g - h_{liq}} \quad (B.8)$$

Under saturated conditions  $h_{liq} = h_f$  and Equation (B.8) is equivalent to the thermodynamic equilibrium quality

$$X_e(z) = \frac{\bar{h}(z) - h_f}{h_g - h_f} = \frac{\bar{h}(z) - h_f}{h_{fg}} \quad (B.9)$$

Also, for saturated conditions, Equation (B.6) can be written

$$X = \frac{h_{in} - h_f}{h_{fg}} + \frac{1}{\dot{m}_{Tot} h_{fg}} \int_0^{z=\xi} \dot{q}'(z) dz \quad (B.10)$$

Equation (B.10) is a function of length (z). For the case where “z” equals the channel exit, the quality becomes the exit quality and the integral term is the total integrated channel power.

$$X_{exit} = \frac{\Delta h_{Sub}}{h_{fg}} + \frac{\dot{Q}}{\dot{m}_{Tot} h_{fg}} \quad (B.11)$$

In this derivation, no assumptions were necessary regarding the void fraction or relative velocities of the phases. Flow quality for the steady state case is determined solely on energy considerations (and conservation of total mass).

## B.2 Void Fraction

A relationship between void fraction and flow quality can be obtained by introducing definitions for the mass flow rates of the phases (using bulk average quantities)

$$\dot{m}_g = \alpha \rho_g \bar{u}_g A \quad \text{and} \quad \dot{m}_f = (1 - \alpha) \rho_f \bar{u}_f A \quad (B.12)$$

Substituting these definitions into Equation (B.5) and rearranging gives

$$\alpha = \frac{1}{1 + \left( \frac{1 - X}{X} \right) \left( \frac{\rho_g}{\rho_f} \right) S} \quad (B.13)$$

where “S” is the slip ratio given by

$$S = \frac{\bar{u}_g}{\bar{u}_f} = \left( \frac{1 - \alpha}{\alpha} \right) \left( \frac{X}{1 - X} \right) \left( \frac{\rho_f}{\rho_g} \right) \quad (B.14)$$



The slip ratio is the ratio of the average velocities of the phases. The drift flux model can be used to provide information about slip

$$\bar{u}_g = C_o j + \bar{v}_{gj} \quad (\text{B.15})$$

where the superficial velocity ( $j$ ) is given by

$$j = j_g + j_f = \alpha \bar{u}_g + (1 - \alpha) \bar{u}_f \quad (\text{B.16})$$

Using the relations in Equation (B.12) the superficial velocity can be written

$$j = \frac{\dot{m}}{A} \left[ \frac{X}{\rho_g} + \frac{(1 - X)}{\rho_f} \right] \quad (\text{B.17})$$

Substituting  $\alpha = X\dot{m}/\rho_g \bar{u}_g A$  (Equation (B.12) again) into Equation (B.14), then using (B.17), (B.15) and rearranging gives [25]

$$S = C_o + \frac{X \rho_f (C_o - 1)}{\rho_g (1 - X)} + \frac{\rho_f \bar{v}_{gj} A}{\dot{m} (1 - X)} \quad (\text{B.18})$$

Recognizing that the last term can be neglected for many conditions of interest, Equation (B.18) allows quick, but reasonably accurate estimates of void fraction (only basic thermal-hydraulic parameters and reasonable estimates of  $C_o$  are required).

### **B.2.1 Upper Range Estimate – GNF2 Data**

Flow (or equilibrium) quality as described by Equation (B.11) varies with subcooling, power, and flow. The first term represents the sensible heat needed to achieve saturation conditions in the bulk liquid. The second term is directly proportional to power, and inversely proportional to mass flow rate. Referring to Figure F-7 for the GNF2 based data, [[

(B.19)

(B.20)

(B.21)

(B.22)

]]

While the pressure drop tests did not measure void fraction directly, the upper range of the test data used for validation can be reasonably estimated without relying on the Findlay-Dix correlation to calculate the value (only reasonable estimates of  $C_o$  are necessary).

### **B.2.2 Upper Range Estimate – GE14 Data**

Repeating the recipe in the previous example, the GE14 pressure drop experiments contained points [[

(B.23)

(B.24)

(B.25)

]]

The void fraction given by this power-to-flow ratio is very high; in fact, it is likely higher than what would commonly be encountered in normal service, where the bundle operating state would be constrained by the Operating Limit MCPR (OLMCPR). Stated a different way, in order to achieve [[ ]], this test bundle's MCPR could have violated the OLMCPR that would limit peak bundle power for an operating reactor. ATLAS Test Assembly 751 (ATA751) was used for both critical power and pressure drop testing. The critical power data for ATA751, peaking patterns B through I indicates that the critical power is very close to [[ ]]

]]

### **B.3 Application to Fuel Simulation**

In general, thermal limits restrict the maximum achievable bundle power in any given core, at any given steady state operating condition. For a given set of thermal-hydraulic conditions, the OLMCPR directly limits the peak power bundle. The LHGR limit applies locally (on a rod and axial node basis) and indirectly limits bundle power by restricting the total peaking (i.e., LHGR effectively limits the allowable the combinations of axial power shapes and radial peaking patterns). Off-rated limits impose additional margin relative to limits applied at rated conditions.

---

<sup>20</sup> Many BWRs operate [[ ]]

]]

Limits developed to comply with ARTS<sup>21</sup> take the most limiting of several parameters, including a flow dependent MCPR (i.e., MCPRF), in order to constrain off-rated operation. An example of MCPRF is shown in Figure B-1.

[[

]]

**Figure B-1 Generic MCPR<sub>F</sub>**

### **B.3.1 Expected Upper Void Fraction Range for Peak Bundles**

The Findlay-Dix correlation can be applied to steady state critical power data in order to examine the expected maximum (exit) void fraction values for 10x10 bundles. Figure B-2 shows channel exit void fraction values predicted using the Findlay-Dix correlation<sup>22</sup> for a set of GNF2 critical power data points. Note that the GNF2 design generally demonstrates higher critical power capability than GE14. Also, the data is for an inlet peaked APS, which maximizes critical power

---

<sup>21</sup> Average Power Range Monitor, Rod Block Monitor, and Technical Specification (ARTS) improvement programs.

<sup>22</sup> The correlation presented in NEDE-21565 is applied with steam properties evaluated at 1,000 psia, i.e., not the “hand calculation” method presented in Sections 0 and 0. Also, the calculated void fractions are referenced to the fully rodged bundle flow area, which slightly over estimates the exit void fraction values.

relative to other axial power distributions (e.g., outlet peaked). Only the [[

]]

The predicted exit void fractions extend to about [[ ]] at very low flow conditions. For bundle power-to-flow ratios less than about 13 MWt/Mlbm/hr-ft<sup>2</sup> (or mass fluxes greater than 0.8 Mlbm/hr-ft<sup>2</sup>), the highest exit void fractions at critical power are about [[ ]]. The onset of Boiling Transition (i.e., “BT” or film dryout) in BWR fuel bundles will occur on a rod (or rods) while other rods remain wetted; liquid inventory will also be available on unheated surfaces (e.g., channel walls) and in the form of droplets entrained in the vapor, so under forced convective conditions, dryout does not correspond to  $\alpha = 1.0$ . For increasing power or heat flux, annular flow will eventually transition to mist flow (post dryout), where significant energy addition may be required to vaporize the remaining liquid.

[[

]]

**Figure B-2 Predicted Exit Void Fractions Based on Critical Power Data**

In Figure B-2, the points marked “Exit Void at MCPR = 1.4” are predicted at the same conditions as the critical power points, only constrained by a MCPR limit. The resulting power levels are reduced relative to critical power and more typical of operation. The reduced power is obtained using the definition of the bundle critical power ratio

$$MCPR = \frac{\text{Critical Power}}{\text{Power}} \quad (\text{B.26})$$

Also, the generic  $MCPR_F$  limit shown in Figure B-1 has been applied, using the approximation that 100% core flow corresponds to 1.0 Mlbm/hr-ft<sup>2</sup> bundle flow, 50% core flow corresponds to 0.5 Mlbm/hr-ft<sup>2</sup> bundle flow, etc., etc. Applying  $MCPR_F$  (using the 102.5% curve) affects the low flow points (e.g., 0.3 Mlbm/hr-ft<sup>2</sup>). The reduced bundle power level becomes

$$\text{Power} = \frac{\text{Critical Power}}{MCPR} = \frac{\text{Critical Power}}{\max(1.4, MCPR_F)} \quad (\text{B.27})$$

As a point of reference, applying the limit  $MCPR = 1.4$  for this bundle design and APS gives a peak bundle power of about [[ ]] at 0.8 Mlbm/hr-ft<sup>2</sup> and 20 Btu/lbm subcooling. This corresponds to a bundle power-to-flow ratio of about 9 MWt/Mlbm/hr-ft<sup>2</sup> and an exit void fraction of slightly less than 92%, as shown in the figure.

This exercise demonstrates that under steady state conditions typical of plant operation, expected values for 10x10 peak bundle maximum (exit) void fraction values are well within the application range of the Findlay-Dix correlation, as well as consistent with the predicted void range for the 10x10  $\Delta P$  data. The range of void fractions in the Findlay-Dix rod data covers from [[

]] It is also worth noting that this discussion is presented in terms of the limiting power envelope represented by bundle critical power data, which is determined from tests, independent of the core operating domain. In other words, the void fraction information presented in this section is derived independent of the explicit core operating state (i.e., relative to a particular core or point on a power-flow map). Thermal limits information combined with bundle power-flow and subcooling information are sufficient for drawing conclusions regarding maximum expected (bundle exit) void fractions applicable to all operating domains.

## APPENDIX C    “METHOD B” PRESSURE DROP

A summary of the standard expressions used to evaluate the pressure drop in a fuel bundle are given in Table C-1. The expressions are [[

**Table C-1    Expressions Applied to Calculate the In-Channel Pressure Drop**

Pressure Drop Term	Expression
Elevation	See Equation (2.11)
Friction	$\Delta P_{Fric} = f \left( \frac{\Delta z}{D_H} \right) \frac{\dot{m}^2}{2g_c \rho_{liq} A^2} \phi_{lo}^2$ <p>The single-phase friction factor (<math>f</math>) is based on a fit to the Moody curves, which are fit to <math>Re</math>, <math>D_H</math>, and surface roughness. [[</p> <p style="text-align: right;">]]</p>

NEDO-33173 Supplement 1, Revision 0  
Non-Proprietary Information

Pressure Drop Term	Expression
Local losses (spacers)	$\Delta P_{Loc} = \left( \frac{k}{A^2} \right) \frac{\dot{m}^2}{2g_c \rho_{liq}} \phi_{TPL}^2$ <p>The two-phase local loss multiplier [[</p> <p style="text-align: right;">]]</p>
Acceleration	$\Delta P_{Acc} = \frac{\dot{m}^2}{g_c A^2} \left[ \frac{1}{\rho_{out}} - \frac{1}{\rho_{in}} \right]$ <p>where the “out” and “in” densities are [[</p> <p style="text-align: right;">]]</p>
Acceleration due to a flow area change	<p style="text-align: center;">[[</p> <p style="text-align: right;">]]</p>



## APPENDIX D      ATLAS MEASUREMENT UNCERTAINTIES

This appendix presents a brief discussion of measurement uncertainties (basic measurement accuracies) associated with the ATLAS facility.

**Table D-1      Measurement Uncertainty Components**

Uncertainty Component	Value
Power (W)	[[
Mass Flow Rate (M)	
Inlet Subcooling (h)	
System Pressure (P)	
Differential Pressure (DP)	]]

The system pressure uncertainty will affect the quality in the channel, which affects the two-phase  $\Delta P$ . Similarly, the temperature uncertainty affects the inlet subcooling and the boiling length in the channel, which affects the two-phase  $\Delta P$ . The mass flow rate uncertainty can be significant, as pressure drop generally varies with the square of the flow rate. The uncertainty associated with the power supply is neglected in this evaluation to ensure that the total error is underestimated. The total measurement uncertainty is a sum of the components in Table D-1.

$$\sigma_{Meas}^2 = \sigma_M^2 + \sigma_h^2 + \sigma_P^2 + \sigma_{DP}^2 + \cancel{\sigma_W^2} \quad (D.1)$$

An estimate of the mass flow rate sensitivity can be obtained from Figure F-3, which shows the slope of measured  $\Delta P$  versus mass flow rate for a series of tests. The family of curves in the figure shows that the slope increases with power due to higher two-phase pressure drops. Estimating the sensitivity based on relatively low power should underestimate the measurement uncertainty, which should (conservatively) overestimate the void uncertainty. [[

(D.2)

(D.3)

]]

The impact of inlet subcooling variation on the measurements is a little more difficult to evaluate. However, estimating the error impact as a change in flow quality allows an equivalent power change to be determined, which can be related to pressure drop through Figure F-3 (consistent with the estimate for the flow rate error). Considering a one-dimensional, steady state mass and energy balance gives an expression for (exit) flow quality (see Appendix B)

$$X = \frac{\Delta h_{Sub}}{h_{fg}} + \frac{\dot{Q}}{\dot{m}h_{fg}} \quad (D.4)$$

An equivalent quality change for a given subcooling change (constant power) can be written

$$\Delta X = \frac{\Delta h_{Sub,1} - \Delta h_{Sub,2}}{h_{fg}} = \frac{\sigma_h}{h_{fg}} \quad (D.5)$$

The resulting quality change can be expressed as an equivalent power change (constant subcooling)

$$\Delta X = \frac{\Delta \dot{Q}}{\dot{m}h_{fg}} \quad (D.6)$$

[[

(D.7)

(D.8)

(D.9)

(D.10)

(D.11)

(D.12)

]] (D.13)

This is an interesting result, in that the magnitude of the measurement uncertainty is relatively small in comparison to the measured pressure drop values [[  
]], but worth consideration relative to the prediction error.

## APPENDIX E STATISTICS

### E.1 Overall Mean and Standard Deviation Based on Subset Values

NEDE-21565 [9] provides summary data, but does not list individual error residuals for all datasets. Therefore, working with this data, it is often necessary to combine subsets of data. In general, a dataset can be composed of “m” subsets, each with their own calculated mean and standard deviation

$$\mu_i = \frac{1}{n_i} \sum_{j=1}^{n_i} x_{i,j} \quad (\text{E.1})$$

$$\sigma_i^2 = \frac{1}{n_i - 1} \sum_{j=1}^{n_i} (x_{i,j} - \mu_i)^2 \quad (\text{E.2})$$

where  $n_i$  is the number of points in each subset and  $x_{i,j}$  are the individual observations. The total number of points in the data set is

$$n = \sum_{i=1}^m n_i \quad (\text{E.3})$$

The mean of the data is given by

$$\mu = \frac{1}{n} \sum_{i=1}^m \sum_{j=1}^{n_i} x_{i,j} = \frac{1}{n} \sum_{i=1}^m n_i \mu_i \quad (\text{E.4})$$

where Equation (E.1) has been used. The standard deviation is given by

$$\sigma^2 = \frac{1}{n - 1} \sum_{i=1}^m \sum_{j=1}^{n_i} (x_{i,j} - \mu)^2 = \frac{1}{n - 1} \sum_{i=1}^m \sum_{j=1}^{n_i} (x_{i,j}^2 - \mu^2) \quad (\text{E.5})$$

Note that the RHS of (E.5) requires a bit of algebra and Equation (E.4). Adding and subtracting  $\mu_i^2$ , summing over “j,” and using Equation (E.2) gives

$$\sigma^2 = \frac{1}{n - 1} \sum_{i=1}^m \left[ (n_i - 1) \sigma_i^2 + n_i (\mu_i^2 - \mu^2) \right] \quad (\text{E.6})$$

Manipulating the far right term in Equation (E.6) and using Equation (E.4) again gives

$$\sigma^2 = \frac{1}{n - 1} \sum_{i=1}^m \left[ (n_i - 1) \sigma_i^2 + n_i (\mu_i - \mu)^2 \right] \quad (\text{E.7})$$

Note that in arriving at Equation (E.7), no assumptions are made about the probability density functions.

## E.2 Tolerance Intervals

### E.2.1 Discussion – Confidence and Tolerance Intervals

It is possible to determine confidence intervals for statistics, such as the mean ( $\mu$ ) and standard deviation ( $\sigma$ ). These intervals essentially enclose these population parameters with a given confidence level. A way to consider these intervals is that if someone were to draw samples from a population, computing  $\bar{x}$  and  $s$  each time, then some percentage of these samples would be likely to contain  $\mu$  and  $\sigma$ . Tolerance intervals are different from confidence intervals. Tolerance intervals are usually constructed from experimental data so as to enclose  $P\%$  or more of the population of points with a given confidence  $1 - \alpha$ . In the case of tolerance intervals, drawing a large number of samples should result in  $100(1 - \alpha)\%$  of the cases sampled enclosing at least  $P\%$  of the population. Reference [33] contains a detailed discussion of confidence and tolerance intervals.

### E.2.2 One-Sided Tolerance

Error residuals for a sample can be defined from

$$\varepsilon_i = X_i^{\text{measured}} - X_i^{\text{predicted}} \quad (\text{E.8})$$

If the error residuals follow a normal distribution, then they may be characterized by a mean error (bias) and standard deviation.

$$\bar{\varepsilon} \pm \sigma \quad (\text{E.9})$$

In this case, from Table 1-2, the mean error and standard deviation for the historical Findlay-Dix database are [[ ]]. With this information, it is possible to define a one-sided upper tolerance limit so that  $100P\%$  of the population is less than  $U$  at the  $1 - \alpha$  confidence level.

$$U = \bar{\varepsilon} + k\sigma \quad (\text{E.10})$$

The tolerance factor [33] is given by

$$k = \frac{K_{1-P} + \sqrt{K_{1-P}^2 - ab}}{a} \quad (\text{E.11})$$

$$a = 1 - \frac{K_\alpha^2}{2(n-1)} \quad (\text{E.12})$$

$$b = K_{1-P}^2 - \frac{K_\alpha^2}{n} \quad (\text{E.13})$$

The cumulative area under the standardized normal curve is used to give the “K-factor” in the above equations. More precisely,  $K$  corresponds to the normal deviate that gives an upper tail area of  $1-P$  or  $\alpha$ . At the 95/95 level,

$$K_{1-P} = K_\alpha = K_{0.05} = 1.645 \quad (\text{E.14})$$

$$[[ \quad \quad \quad ]] \quad (E.15)$$

$$(E.16)$$

$$(E.17)$$

$$]] \quad (E.18)$$

If additional samples are drawn from the same population, one should expect that 95% of the void comparisons would underpredict  $\alpha$  less than  $[[ \quad \quad \quad ]]$  95% of the time.

### E.2.3 Two-Sided Tolerance Interval

Similarly, a two-side interval can be constructed

$$TI = \bar{\varepsilon} \pm k\sigma \quad (E.19)$$

In this case, given the large number of points in the population,  $k$  can be taken as 1.96 (the standard deviate  $z = 2$  for a normal population). Using this approximation for  $k$ , the resulting interval is

$$[[ \quad \quad \quad ]] \quad (E.20)$$

Given this interval, 95% of the samples drawn from this population of error residuals ( $\varepsilon_i$ ) would be expected to lie between  $[[ \quad \quad \quad ]]$ , 95% of the time.

## APPENDIX F      ERROR RESIDUALS AT HIGH FLOW RATES

### F.1      Discussion

Consistent with the low flow evaluation in Section 2.3, the approach taken in Section 2.4 to assign all net error to the void / elevation term. At the higher flow rates, the residual errors tend to be dominated by the non-void related terms

$$\underbrace{\left| \frac{1}{n} \sum_i^n (\delta P_i^{Acc} + \delta P_i^{Fric} + \delta P_i^{Loc}) \right|}_{\substack{\text{Average error for calculated terms} \\ \text{proportional to the square of mass} \\ \text{flux } (\Delta P \propto G^2)}} \geq \underbrace{\left| \frac{1}{n} \sum_i^n \delta P_i^{Elev} \right|}_{\substack{\text{Average error for} \\ \text{calculated term} \\ \text{proportional to void} \\ \text{fraction } (\Delta P \propto \alpha)}} \quad (F.1)$$

Using this approach, the void fraction contribution to the net or average error residual is overestimated.

Equation (F.1) can be examined in simple terms, for example, the maximum available  $\Delta P_{elev}$  is the difference between a column of liquid versus a column of vapor, which is only about 3.8 psid (0.03 kPa) under typical BWR conditions. Void fraction errors can only impact this relatively small constituent of the total  $\Delta P_{Calc}$  (i.e., 3.8 compared to a total pressure drop of 10 to 20 psid, or 0.07 to 0.14 kPa from Figure F-3). Given that the residual errors ( $\delta P$ ) will be some proportion of the constituents, the error potential is much larger for the frictional terms.

The calculated frictional losses (i.e., acceleration, friction, and local losses) are correlated to the square of mass flux, as shown in Appendix C. The calculated elevation loss is proportional to void fraction, which directly relates to quality or power-to-flow ratio (Appendix B). Given this information, the validity of Equation (F.1) can be examined through trend and correlation analyses.

### F.2      Trend Analysis

Figure F-3 (GE14) shows an example of measured versus calculated  $\Delta P$  as a function of mass flux. Various power-to-flow ratios (quality distributions) are presented. The figure shows a slight trend with mass flux. Close examination of the figure indicates that the “Method B” equation set (Appendix C) [[

]]

[[

]]

**Figure F-3    Predicted GE14 Bundle Pressure Drops Versus Data**



### F.3 Correlation Analysis

The residual errors ( $\Delta P$ ) can be fit to parameters such as mass flux and power-to-flow ratio (proportional to exit or average void fraction). The degree of correlation (goodness of fit characterized by  $r^2$ ) can be taken as evidence of a relationship, or a lack of a relationship. Correlation analysis does not imply causality or reveal underlying reasons for causal relationships, but can be used to determine when relationships exist.

[[

]]

Elevation pressure drop decreases linearly with increasing void fraction, as shown by Equation (2.11). Simply stated, a column of solid water weighs more than a column of vapor, and the intermediate states are a simple linear function of the volume fraction. Using saturated fluid properties at 1,000 psia (6.89 MPa), a  $\delta P = 0.19$  psid measured error equates to a  $\Delta\alpha = 0.05$  calculated error regardless of the average void fraction in the fuel bundle (e.g., at either 10% or 90% void fraction). In other words, given the relationship between  $\Delta P_{Elev}$  and  $\alpha$ , residual errors ( $\delta P$ ) are not amplified or distorted by the function  $\Delta P_{Elev} = f(\alpha, \rho, z, g)$ . Furthermore, actual void fraction error can only enter into the residual error ( $\delta P$ ) through this term, because other  $\Delta P$  terms are based on quality. If calculated void fraction error is the source of residual pressure drop error, then based on Figure F-5, the mass flux dependency must also translate to a trend with quality (or power-to-flow ratio). However, this is not the case. [[

]]

[[

]]

**Figure F-4    Pressure Drop Residual Error ( $\delta P$ ) Versus Power-to-Flow Ratio**

[[

]]

**Figure F-5 Pressure Drop Residual Error ( $\delta P$ ) Versus Mass Flux (G)**

**F.4 Integral Versus Local Errors**

The low flow comparisons shown in Section 2.3 indicate good agreement over the various axial segments within single test runs. The comparisons agree well at the various steam qualities encountered (axially) within the test bundles. This is shown graphically in Figure F-6, which shows axial pressure drop and void fraction profiles for several of the tests given in Table 1-1. Similarly, tests at higher flow rates also agree axially; an example is shown in Figure F-7. Note that this particular test is a high power-to-flow ratio case and is discussed in Appendix B. Given the good axial agreement, for convenience, the results in Section 2.4.2 are presented in terms bundle pressure drop values (i.e., a single  $\delta P$  and  $\delta \alpha$  for each experimental run that represents the entire test section).

[[

]]

**Figure F-6    Pressure Drop and Void Fraction for Selected GNF2 Low Flow Tests**

[[

]]

**Figure F-7     Pressure Drop and Void Fraction for a High Exit Quality (Higher Flow) Test**